Check for updates

APPLIED SCIENCES AND ENGINEERING

Machining swarf formation–inspired fabrication of ferrofluidic helical miniature robots with multimodal locomotion capability

Xinjian Fan[1]†, Qinkai Chen[2]†, Mingtong Li[3]†, Zhengnan Wu[1], Dingwen Tong[2], Hui Xie[4], Zhan Yang[1]*, Lining Sun[1]*, Metin Sitti[3,5]*

Copyright © 2025 The Authors, some rights reserved; exclusive licensee American Association for the Advancement of Science. No claim to original U.S. Government Works. Distributed under a Creative Commons Attribution NonCommercial License 4.0 (CC BY-NC).

Magnetic helical robots (MHRs) have shown notable potential for targeted therapy. However, traditional fabrication methods are usually complex and expensive, and the prepared MHR's locomotion is monotonous with limited capacity. Here, we present a cost-effective, customizable, and scalable fabrication craft of MHR, via using bent needle tips to engrave helical structures onto polymethyl methacrylate substrates and incorporating nanoparticle alignment strategies to create ferrofluidic helical miniature robots (FHMRs) with cross-scale size scopes. We then propose strategic magnetic driving methods that enable FHMRs with five powerful motion modes for negotiating various application scenarios. Experimental results show that FHMRs can move flexibly and effectively simulate thrombus removal within a vascular model by integrating multiple motion modes. Furthermore, modified FHMRs can swiftly deliver drugs to targeted areas, with the capability for phased release on surfaces of wrinkled physiological tissues. These advancements highlight the considerable potential of FHMRs for future applications in the biomedical field.

INTRODUCTION

In recent years, magnetic microrobots have garnered considerable attention as an innovative transformative technology with the potential to revolutionize targeted drug delivery (*1*–*5*), cell capture (*6*), and environmental remediation (*7*, *8*). These miniature robotic systems have the unique capability to navigate confined spaces and perform complex tasks while minimizing interference with the surrounding environment and human body (*9*). Particularly, magnetic helical robots (MHRs), inspired by the rotating helical flagella of bacteria, combine the dual advantages of magnetic field actuation and helical propulsion (*10*). By converting rotational motion induced by a magnetic field into linear motion, MHRs facilitate efficient locomotion in various media, such as fluids and soft tissues (*11*–*14*). Moreover, these microrobots can be wirelessly maneuvered and omnidirectionally steered using external magnetic fields (*15*–*17*). Peyer *et al.* (*18*) demonstrated that helical microrobots are capable of achieving stable spiral propulsion under magnetic actuation in various liquids and tissues. The intrinsic properties of MHRs are highly compatible with complex biological environments, allowing them to effectively navigate through biological fluids and tissues and avoid obstacles (*19*, *20*). These microrobots are emerging as a valuable technology in the biomedical field, becoming a substantial research focus and an effective platform for achieving targeted drug delivery and performing minimally invasive medical procedures (*21*–*23*).

For example, many research groups have explored the manufacturing methods and motility of MHRs, presenting a range of intriguing experimental results. In terms of MHR fabrication methods, Qiu *et al.* (*24*) developed artificial bacterial flagella helices using the biocompatible photoresist ORMOCOMP and coated them with thin iron films through electron beam deposition, achieving the preparation of MHRs. Subsequently, Qiu *et al.* (*11*) innovatively used a three-dimensional (3D) laser direct writing tool and electron beam deposition methods to fabricate MHRs with a dual-layer coating of Ni and Ti. This design enabled magnetic actuation through the Ni layer, while the Ti layer enhanced biocompatibility. Venugopalan *et al.* (*25*) used glancing angle deposition to fabricate helical structures on a SiO_2 substrate and used a microwave-assisted chemical synthesis method to form conformal zinc ferrite coatings on the helices. After ultrasonic treatment, they achieved long-term magnetic actuation of micron-scale MHRs in a blood environment. The bio-template methods, such as the spirulina platensis (*26*), are promising for the scalable fabrication of helical structures that rely on microbial self-replication, and their inherent biodegradability enables natural decomposition in physiological environments with no long-term retention risks. The bio-template methods proposed have extremely enhanced the potential of biomedical applications. However, these methods, such as 3D printing, electrodeposition, and two-photon polymerization (TPL), are plagued by issues, including complex procedures, lengthy production cycles, high development thresholds, and substantial costs (*27*–*29*). In addition, the biological template method is limited by the inherent non-customizability of the biological templates used and the difficulty in adjusting scales, making it unsuitable for task-specific customization and adaptation to different chemical environments (*30*–*33*). These challenges limit the accessibility and scalability of MHRs (*34*). Considering the aforementioned constraints and the evident requirement for targeted drug delivery in complex biological environments, the design of MHRs must be adaptable to diverse conditions (*35*). Therefore, a facile manufacturing approach that is straightforward, cost-effective, tran-scalable, and adaptable to specific requirements is essential.

Besides, in complex human environments, MHRs must intelligently interact with their surroundings and perform tasks with high

[1]School of Mechanical and Electrical Engineering, Soochow University, No. 8, Jixue Road, Suzhou 215131, China. [2]School of Future Science and Engineering, Soochow University, No.1, Jiuyong West Road, Suzhou 215222, China. [3]Physical Intelligence Department, Max Planck Institute for Intelligent Systems, Heisenbergstr. 3, Stuttgart 70569, Germany. [4]State Key Laboratory of Robotics and Systems, Harbin Institute of Technology, Yikuang, Harbin 150080, China. [5]School of Medicine and College of Engineering, Koç University, 34450 Istanbul, Turkey.
*Corresponding author. Email: yangzhan@suda.edu.cn (Z.Y.); lnsun@hit.edu.cn (L.S.); sitti@is.mpg.de (M.S.)
†These authors contributed equally to this work.

Downloaded from https://www.science.org at Koc Universitesi Suna Kirac on December 05, 2025

precision, substantially increasing their control complexity (*36*). Sun *et al.* (*37*) achieved precise control over NC/Fe_3O_4 microgenerators through remote magnetic manipulation, enabling targeted delivery of anticancer drugs. Similarly, Dong *et al.* (*38*) developed an endoscope-assisted therapeutic platform using oscillating Fe_3O_4 helical micromachines with peroxidase-mimicking catalytic activity, which effectively treated biofilm-associated infections in a T-shaped tube. Lee *et al.* (*39*) designed helical microstructures using a polymer on the basis of polyethylene glycol diacrylate fabricated through two-photon lithography, enabling not only targeted drug delivery but also biodegradation posttreatment. These studies have advanced MHR control strategies and broadened their biomedical applications. However, in highly variable environments or complex terrain, such as the viscous fluids and folds of the human stomach, the single-mode motion of MHRs in these approaches proves to be limiting (*40*). In complex human environments, MHRs must interact with their surroundings and perform tasks with high precision, which substantially complicates their control (*41*). Therefore, addressing issues related to multimodal locomotion control, such as dynamic control, stability, multimodal coordination, and functionalization, is essential (*42*), which will enhance their adaptability and performance across a wide range of potential applications (*43*–*46*).

To address these limitations, we introduced a facile fabrication craft to create ferrofluidic helical miniature robots (FHMRs) inspired by the process of machining swarf formation, along with a multimodal locomotion control strategy. This approach leverages a bent needle tip to cut and sculpt on a polymethyl methacrylate (PMMA) substrate. A multi-degree-of-freedom, adjustable-parameter fabrication platform is designed, allowing customization of the relative position and orientation between the needle tip and the substrate during manufacturing, as illustrated in Fig. 1A. Furthermore, we propose a reconfigurable encoding mechanism on the basis of ferrofluid curing and dissolution, achieved through solvent evaporation, as shown in Fig. 1B. This method enables reconfiguration of the nanoparticles' alignment along either the long or short axis, while the biocompatibility of PMMA and the ferrofluid ensures minimal biocompatibility issues. In addition, as illustrated in Fig. 1C, to implement a multimodal locomotion control strategy for FHMRs, we constructed an OctoMag-like multidirectional magnetic control system (*47*). The specific diagram of the magnetic control system and the magnetic field data for a single electromagnetic coil can be found in figs. S1 and S2. The system enables easy generation of magnetic fields up to 20 mT, typically used in experimental settings, at the workspace center. Building upon this foundation, as illustrated in Fig. 1D, we have demonstrated five distinct locomotion modes of FHMRs for negotiating various application scenarios. These modes include the rolling, swing, and rising modes of the short-axis ferrofluidic helical robots (SFHRs), as well as the rotation and swing modes of the long-axis ferrofluidic helical robot (LFHR). This multimodal control-ability allows the FHMRs to adapt their motion patterns in response to changing internal environments, expanding their operational scenarios, and enhancing their functional applications. Moreover, to verify the efficacy of different modalities and their combinations in addressing various scenarios and applications, we present a series of motion control demonstrations and application cases. As demonstrated in Fig. 1 (E to G), FHMRs exhibit the capability to clear simulated thrombi within blood vessels, perform adaptive locomotion in nonplanar environments, and navigate through 3D vascular systems. These functions are enabled by the swing, rolling, and rising modes of the SFHR. Furthermore, as illustrated in Fig. 1 (H and I), FHMRs use the rotation and swing modes of the LFHR to locate lesions and deliver targeted therapy in complex biological environments, such as the folded surfaces of the stomach. On the basis these capabilities, we propose a controllable drug delivery strategy using FHMRs with differential control strategy. This method enables FHMRs to rapidly and precisely release drugs in complex wrinkled environments. Additionally, to minimize drug loss, we introduce a drug sustained-release strategy via on-demand adjusting FHMR's motion modes and featuring a polyvinyl alcohol (PVA) protective layer, leveraging its slow water solubility. This method enhances the controllability and operational duration of targeted drug delivery. These cases extensively demonstrate the robust controllability of the FHMRs designed in this study and the adaptability of multimodal FHMRs within the complex environments of biological systems. With these proof-of-concept results, FHMRs hold high potential for future functional biomedical applications in biological environments characterized by notable structural variability.

RESULTS

Fabrication of the FHMRs inspired by machining swarf formation

The traditional manufacturing process of MHR typically faces challenges such as expensive equipment, complex operations, and insufficient adaptability to the multiscale and microstructural environmental variations within biological systems. Therefore, developing a cost-effective, scalable, and customizable fabrication method with rapid environmental adaptability is a critical prerequisite and pressing challenge for the application of MHRs in biomedicine. To address these issues, we drew inspiration from the helical chip formation phenomenon observed during the machining swarf and proposed a facile method for fabricating the helical structure of FHMR. As illustrated in Fig. 2A, we developed a multi-degree-of-freedom parameterized fabrication platform, whose key components include a linear translation stage, a steering engine, and a micro-engraving needle. By applying vertical and lateral forces to form a C-shaped micro-needle tip structure and precisely controlling the movement of the needle tip along the substrate using the linear translation stage, combined with the C-shaped blade-like geometry of the syringe needle and adjustments to the force exerted on the PMMA, we simulated the machining swarf process of metal helical chip formation and generated helical structures (movie S1). However, manually fabricated helical structures often suffer from uneven pitch and diameter due to human factors. In contrast, by using the multi-degree-of-freedom parameterized platform, we were able to fabricate uniform helical microneedle-etched microrobots (HMRs) (Fig. 2B and movie S1). In addition, this platform enables the customizable control of multiple variables and precise regulation of the fabrication process, facilitating the generation of helical structures in various shapes (Fig. 2C).

For example, the size of the helix is closely related to the diameter of the needle. A larger needle diameter results in a larger C-shaped structure, deeper cuts, and, consequently, a larger helix with detailed pitch and helical diameter. The detailed pitch λ and helical diameter is shown in Fig. 2 (D and E). With the pitch angle θ (the angle between the needle and the substrate) fixed at 60°, only the needle diameter is adjusted. Needles with diameters of 0.6, 0.9, 1.2, and 1.6 mm produced helical structures with corresponding diameters of ~0.4, 0.7, 1.1, and 1.6 mm, as shown in Fig. 2F. By varying the needle diameter, helices spanning micrometer scale to millimeter scale are

Downloaded from https://www.science.org at Koc Universitesi Suna Kirac on December 05, 2025

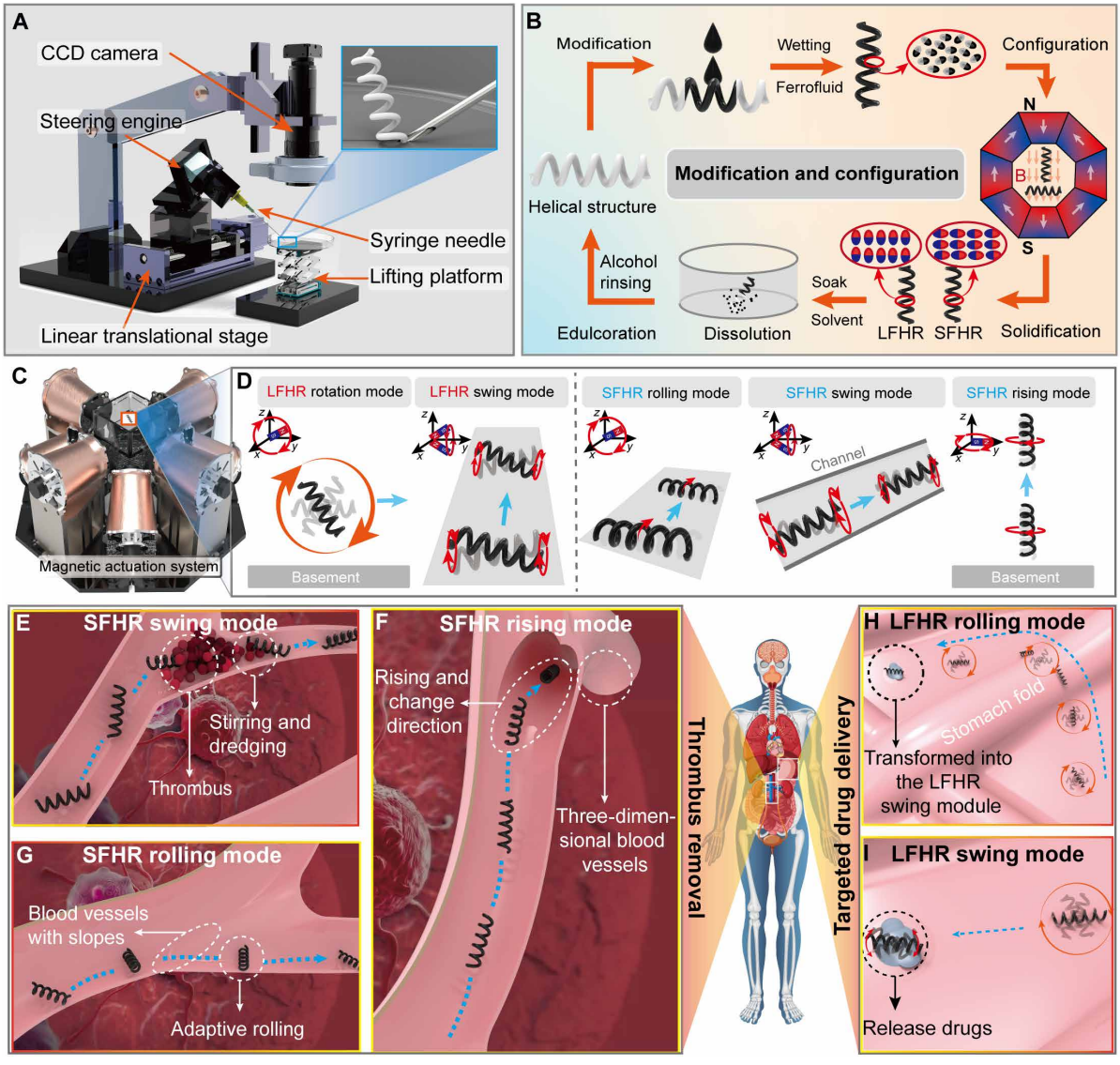


Fig. 1. Overview of fabrication and multimodal locomotion of the FHMR. (**A**) The automatic fabrication devices and the concept picture of the FHMR before configuration. (**B**) The flowchart of the FHMR configuration and reconfiguration process. N represents the north pole of the magnet, S denotes the south pole of the magnet, and B signifies the external magnetic field applied during magnetization. (**C**) Photo of the OctoMag-like magnetic control system. (**D**) The motion states under the five different locomotion modes include the long-axis ferrofluidic helical robot (LFHR) rotation mode, the LFHR swing mode, the short-axis ferrofluidic helical robot (SFHR) rolling mode, the SFHR swing mode, and the SFHR rising mode. (**E**) SFHR crosses and dredges the thrombus in swing mode. (**F**) SFHR moves through the 3D blood vessel in rising mode. (**G**) SFHR moves in the blood vessel with slopes in rolling mode. (**H**) LFHR uses rolling and swing mode crossing the stomach fold and achieving targeting drug delivery. (**I**) LFHR uses swing mode release the drug on the targeted point.

successfully fabricated, as demonstrated in fig. S3. This confirms that the geometric parameters of the helices (pitch and diameter) are directly governed by the needle's geometric design. The current minimum achievable feature size (~70 μm) is constrained by the limited availability of needles, as shown in fig. S4. However, a reduction in helical diameter leads to diminished overall robot volume and insufficient drug-loading capacity, potentially failing to meet targeted therapeutic requirements. Conversely, larger-dimension FHMRs maintain stable propulsion in high-viscosity biological media while exhibiting enhanced drug-loading capacity through an optimized surface-area-to-volume ratio (*48*, *49*). To reconcile this trade-off between bio-navigational capability and therapeutic payload, a needle tip with a 0.6-mm diameter was selected as the fabrication tool, ensuring balanced performance in complex biological environments. This choice enables the fabrication of helical structures with diameters ranging from 100 to 600 μm and pitch range from 100 to 800 μm, which meet the experimental requirements (Fig. 2, D and E). In addition to the needle diameter influencing the size of the helical structure, we also discovered that altering the pitch angle θ (the angle between the needle and the substrate) can adjust the pitch and diameter of the FHMR through experiments, thus providing an innovative method for the customized preparation of FHMRs (Fig. 2C).

To theoretically analyze the influence of the preparation parameter θ on the FHMR structure and elucidate the underlying mechanisms,

Downloaded from https://www.science.org at Koc Universitesi Suna Kirac on December 05, 2025

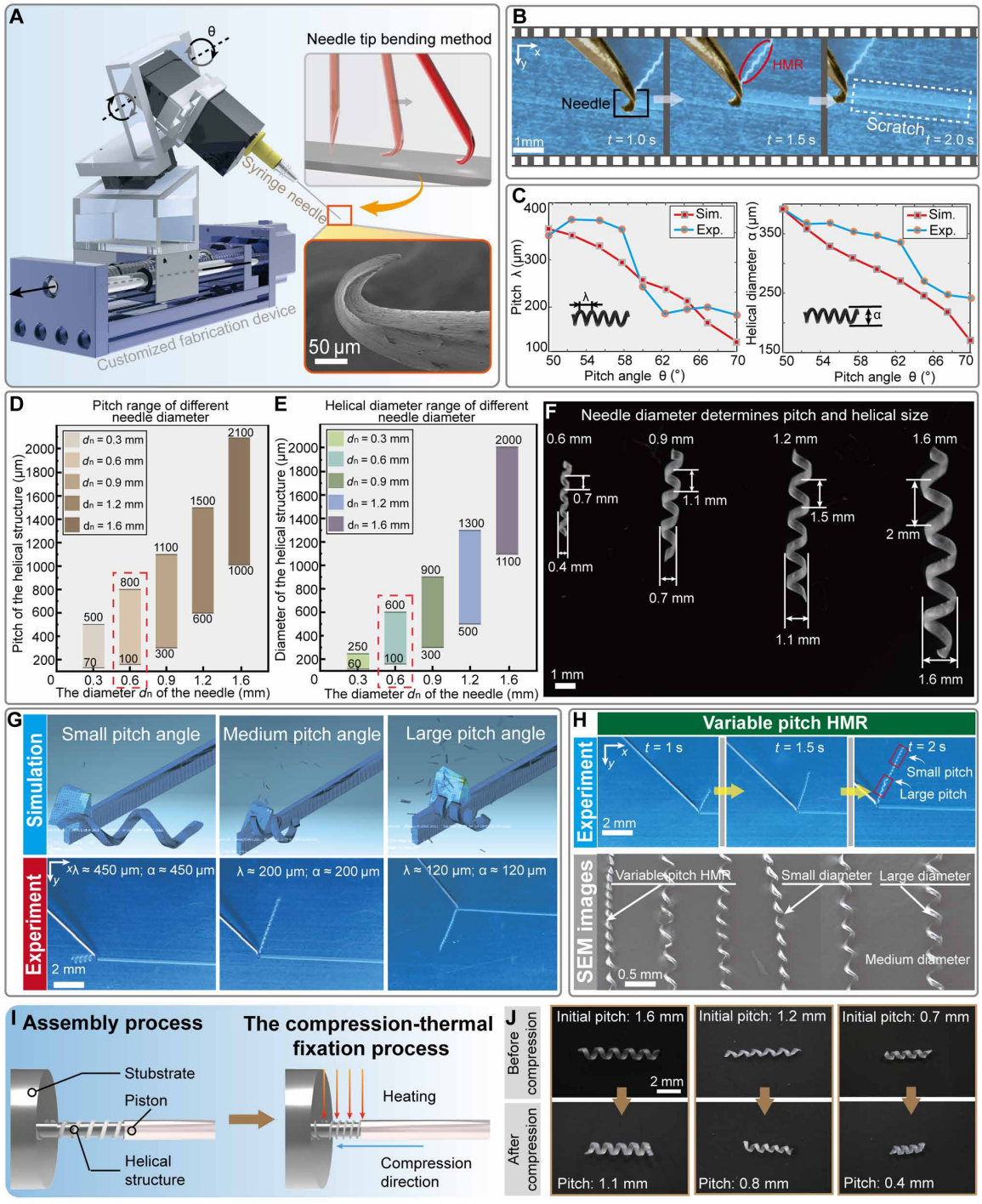


Fig. 2. Fabrication and characterization of FHMR. (**A**) The schematic diagram of fabrication device includes three-axis rotating fabrication system of HMR and the θ is the pitch angle that is the angle between needle tip and substrate, preparation process of bent needle tip, and the structural diagram of bent needle tip under scanning electron microscope (SEM). (**B**) The fabrication process of HMR. (**C**) The left figure shows the relationship between different pitch angle θ and the pitch of HMR, and the right figure shows the relationship between different pitch angles θ and the screw diameter of HMR. The subgraphs show the schematic diagram of HMR pitch and diameter. (**D**) The range of the pitch of helical structures achievable using needle tips with different diameters. The red dashed line represents the needle diameter of 0.6 mm that we selected in the experiment. (**E**) The range of the diameter of helical structures achievable using needle tips with different diameters. (**F**) Different pitches and helical diameters fabricating through different needles. During the fabrication process, the pitch angle was fixed. The figure was captured using a macro camera with ×2 magnification (**G**) The pictures show the different pitch and diameter of the HMR simulation and experimental results for small, medium, and large pitch angles. (**H**) The fabrication process of HMR with substantial changes in pitch and diameter and the SEM images of HMRs with different diameters and variable pitches prepared. (**I**) Active regulation of the helical pitch is achieved through the compression-thermal fixation strategy, and the flowchart illustrates the process from assembly to final structural formation. (**J**) A comparison of the pitch changes between the original helical structure and the structure after compression-thermal fixation.

Downloaded from https://www.science.org at Koc Universitesi Suna Kirac on December 05, 2025

we simulated the effect of the pitch angle θ on HMRs formation using the Johnson-Cook material yield model and the Johnson-Cook material failure model (Eqs. 14 and 15 in the "Simulation Model of FHMR fabrication process" section) through ABAQUS finite element software (movie S1). The simulation started with an initial pitch angle of 50° and increased to 70° in 2.5° increments. As shown in the comparison between the simulation results and experimental validation in Fig. 2G, the pitch λ of FHMRs decreases as the pitch angle θ between the tool and the workpiece increases. Conversely, as the θ increases, the diameter of the FHMRs also decreases. The experimental and simulation parameters are shown in Fig. 2C, the trend of HMR pitch and diameter with the change in θ aligns closely with the simulation results. According to the force analysis of the cutting process described in Supplementary Text S1, this increase in θ subsequently leads to elevated friction and shear forces during the cutting process, which causes the cutting path on the PMMA surface to become steeper. This phenomenon can be explained by the following mechanism: Such a change generally reduces the linear feed rate of the cutting process, as the needle tip penetrates the material at a steeper angle, thereby shortening the cutting path per unit feed distance, resulting in a smaller pitch λ. Furthermore, as the pitch angle increases, the needle's cutting edge penetrates the workpiece more steeply. This greater inclination angle concentrates the applied force in the vertical direction rather than expanding it along the material surface. This concentrated force leads to greater material removal in the vertical direction while the radial cutting is reduced, ultimately resulting in a smaller helix diameter. By adjusting the pitch angle θ, we can precisely control the structure of the HMRs. On the basis of this mechanism, we successfully controlled the fabrication of HMRs with variable pitch λ and diameter, as shown in movie S1. The validity of this mechanism is further confirmed by the experimental results, and the structures of HMRs with different pitches and diameters are shown in Fig. 2H.

Despite the capability of the previously described method to regulate the geometric parameters of helical structures to a certain extent, it falls short of achieving complete decoupling of pitch λ and diameter. To overcome this limitation, we have devised a post-processing technique called compression-thermal fixation strategy. As shown in Fig. 2I, this method entails axially compressing the as-fabricated helical structure followed by thermal annealing to irreversibly stabilize its reconfigured geometry. By exploiting the thermoplastic properties inherent to the material, this approach affords independent and precise manipulation of both pitch and diameter. As shown in Fig. 2J, helical structures processed via the compression-thermal fixation strategy exhibit a consistent and stable reduction in pitch λ relative to their initial dimensions. This observation underscores the method's capacity for controlled pitch modulation. Detailed schematics of the compression apparatus and the fabrication procedure are provided in fig. S5 and movie S2. When combined with the C-shaped tip scribing strategy, such as adjusting the roll or pitch angle θ of the needle, this process enables the creation of helices with customizable pitch-diameter combinations. It is worth noting that the fabrication substrate can be tailored to specific task requirements, enabling the production of helical structures from a diverse range of materials. Notably, PMMA stands out in microrobotic targeted drug delivery due to its exceptional biocompatibility, robust mechanical strength, high hardness, and resistance to various chemical agents. Furthermore, this method exhibits excellent compatibility with a broad spectrum of materials, including polymers with comparable properties, such as polylactic acid and PVA, as detailed in fig. S6.

Programmable nanoparticle alignment method for FHMR

After constructing the helical structure using the multi-degree-of-freedom fabrication platform, a layer of ferrofluid needs to be attached to the surface of the structure before functionalization. Figure 3A demonstrates the attachment process and reconfiguration process of the HMR. By placing the HMR in an external magnetic field of 100 mT applied in different directions, the nanoparticles in the ferrofluid are aligned in an ordered manner. After staying in the magnetic field for 15 min, the ferrofluid gradually dries, and the magnetic particles retain their aligned structure, adhering to the surface of the HMR, thereby completing the attachment process. When reconfiguring the arrangement of the magnetic particles is required, the initial ferrofluid attachment can be stripped under conditions of chemical solvents and ultrasonic assistance, followed by alcohol rinsing and repetition of the above steps to rearrange magnetic particles.

As shown in Fig. 3B, the ferrofluid used consists of Fe_3O_4 nanoparticles with a diameter of ~10 nm, carrier liquid, and surfactant. Fe_3O_4 nanoparticles are soft magnetic materials with superparamagnetism, and their strong magnetism can be shown in Fig. 3C. Besides, the adsorption affinity between ferrofluid and PMMA substrates was experimentally validated through dynamic contact angle analysis. As shown in Fig. 3D, the ferrofluid exhibited rapid wetting behavior on PMMA surfaces, with the contact area expanding substantially within 1 s of deposition. According to the contact angle formula: $\cos\alpha = \frac{\gamma_{SV} - \gamma_{SL}}{\gamma_{LV}}$, a low contact angle indicates stronger adhesion capacity (*50*, *51*), which promotes the expansion of magnetic fluid on the PMMA surface, where α is the contact angle, γ_{SV} is the surface tension between solids and gases, γ_{SL} is the surface tension between solids and liquids, and γ_{LV} is the surface tension between liquid and gas. Contact angle dynamics followed an exponential decay trend, decreasing to ~10°, which is a value indicative of strong interfacial adhesion (Fig. 3E). The chemical interaction between these modified molecules and the PMMA surface promotes the adhesion capacity of particles on PMMA. In addition, analysis of SEM images of the HMRs, as shown in fig. S7 reveals that the manufacturing process yields a textured surface characterized by small pores and subtle undulations. This microstructured surface not only increases the contact area but also enhances capillary action, thereby improving the wettability of magnetic fluids on the robot's body.

It is essential to note that the magnetization process of FHMR necessitates a strong magnetic field, ~100 mT. Generating such a potent magnetic field usually results in a substantial magnetic field gradient, which notably affects the fabrication performance and characteristics of FHMRs, which may lead to uneven distribution of ferrofluid on the surface of HMR and, ultimately, impair the robot's locomotion performance. To address this issue, we have strategically implemented a Halbach magnetization array. The advantage of the Halbach array lies in its ability to produce a relatively uniform internal magnetic field, which is particularly beneficial in mitigating the magnetophoretic effects of the ferrofluid and achieving uniform configuration of the HMRs. By aligning the robot's long axis or short axis parallel to the external magnetic field, we can fabricate robots with completely different operational behaviors. This is primarily due to the differing arrangement of magnetic particles inside the robot during the drying process, resulting from the different configurations.

Downloaded from https://www.science.org at Koc Universitesi Suna Kirac on December 05, 2025

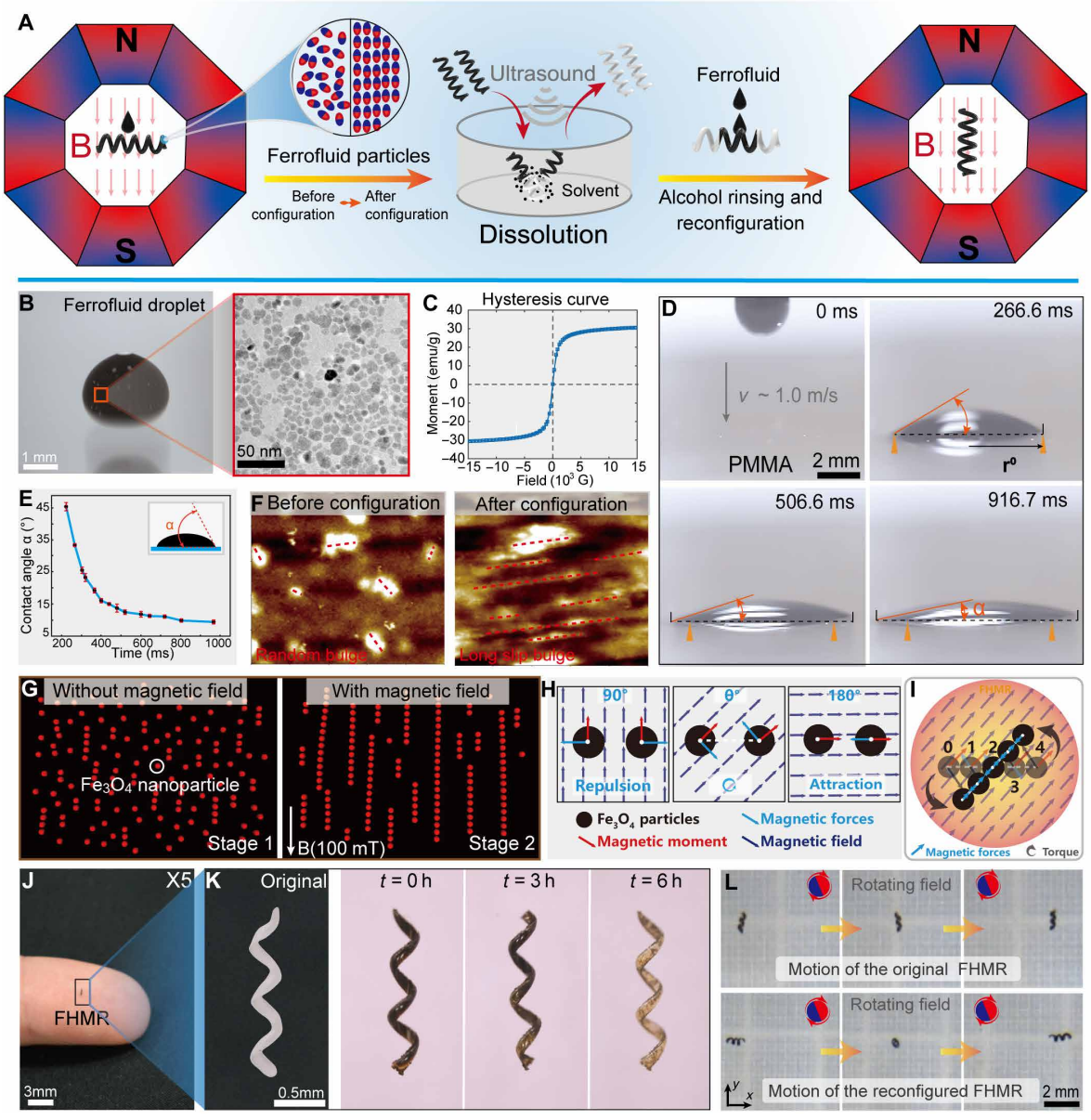


Fig. 3. FHMR configuration full cycle process and the robot performance with different magnetization directions. (**A**) The flowchart of the FHMR configuration and reconfiguration process. (**B**) The photo of the ferrofluid and the SEM imaging results of the nanoparticles in the ferrofluid. (**C**) Hysteresis curve of oil-based ferrofluid at room temperature. (**D**) The contact area of ferrofluid with PMMA material dropped on the material at a speed of 1 m/s within 1 s. (**E**) The contact angle between the ferrofluid and PMMA. (**F**) Surface morphology comparison. Ferrofluid before configuration has random protrusions marked by a red dotted line. Ferrofluid after configuration showing aligned chain-like structures. (**G**) Simulation showing Fe_3O_4 nanoparticles in a ferrofluid forming chain-like structures under a uniform magnetic field. (**H**) Interaction between two fixed Fe_3O_4 nanoparticles under a rotating magnetic field. (**I**) Torque-induced rotation of the nanoparticle chain until alignment with the field. (**J**) Comparison of length of 2-mm FHMR with fingertip. (**K**) The origin state of the helical structural before configuration and the different state of the FHMR at 0, 3, and 6 hours in the FHMR reconfiguration process. h, hours. (**L**) Comparison of motion feedback of FHMR in the same circular rotation magnetic field after different configuration methods. The error bars in (E) are the SDs calculated from three experiments.

Upon the application of an external magnetic field, the superparamagnetic Fe_3O_4 nanoparticles in the ferrofluid are reoriented and aggregated into chain-like structures aligned with the applied field. During the drying process, the oil-based carrier evaporates, locking these chain-like structures onto the surface of the HMR. This alignment minimizes the system's magnetic potential energy (*34*). To characterize this effect, we used atomic force microscopy to examine the surface morphology of ferrofluid dried on a 50 μm–by–50 μm area under two conditions. As shown in Fig. 3F, the ferrofluid without magnetic field effect exhibits no distinct chain-like protrusions, and its shape is relatively random, with the long-axis direction being chaotic and the distribution of Fe_3O_4 nanoparticles remaining relatively flat. In contrast, the ferrofluid affected by the magnetic field shows distinct chain-like protrusions, with orientations tightly aligned

Downloaded from https://www.science.org at Koc Universitesi Suna Kirac on December 05, 2025

to the magnetic field direction. Furthermore, simulations were used to validate this (Fig. 3G and movie S3), treating each Fe_3O_4 nanoparticle as an independent magnetic dipole under the external magnetic field. The simulation results further indicate that the Fe_3O_4 nanoparticles form chains aligned with the external magnetic field. The specific formation mechanism of internal Fe_3O_4 nanoparticle chains is shown in Supplementary Text S2. Furthermore, simulations of two Fe_3O_4 nanoparticles fixed in space under a rotating magnetic field (Fig. 3H, fig. S8, and movie S3) show that, when their alignment deviates from the magnetic field direction, magnetic interactions drive them to realign (*52*). Extending this to a chain of five fixed nanoparticles, on the basis of simulations of interactions between two Fe_3O_4 nanoparticles with fixed spatial positions, we further provided the internal interactions and overall forces of nanoparticles arranged in a chain under the influence of an external magnetic field. As shown in Fig. 3I, under the influence of an external magnetic field, the entire chain will experience a counterclockwise magnetic torque, leading to rotational motion until the extension direction of the chain structure aligns with the direction of the external magnetic field. As all chain structures within the robot experience a uniform torque direction, the entire robot moves along either the long or short axis depending on how it is configured, as shown in fig. S9. For a detailed explanation of the directional rotational motion mechanism of the FHMR, refer to Supplementary Text S3.

The above analysis indicates that the magnetic response behavior of robots is governed by the configuration of internal magnetic nanoparticles. Therefore, the motion modes of FHMRs can be redefined by reconfiguring these nanoparticles. The specific steps are as follows: During the reconfiguration process, the previous FHMRs (Fig. 3J) are placed in the cyclohexane and assisted by an ultrasound field to aid in the detachment of Fe_3O_4 nanoparticles. The separation effect is demonstrated in Fig. 3K. After 3 hours, the magnetic particles start to peel off. After 6 hours, a large amount of particles peel off. We selected six points on FHMR at different times to evaluate the reconfiguration effect on the basis of the average grayscale value, as shown in fig. S10. Here, we chose cyclohexane as the solvent for demagnetizing FHMR due to its similar solubility characteristics and balanced polarity and hydrophobicity, which allows it to interact with oil-based carrier liquids in ferrofluid, thus being able to dissolve weakly polar or nonpolar oil-based fluids, ultimately reducing the viscosity of ferrofluid and helping to dissolve and disperse them (*53*, *54*). After peeling off the ferrofluid layer, we rinse the FHMR surface with alcohol to ensure the removal of any residual solvent. The reconfiguration process is identical to the previous method, except for the difference in the direction of the HMR's long axis. Experiments show that when the nanoparticles are aligned laterally, the robot can move in response to an external rotating magnetic field. After reconfiguring the nanoparticles to align longitudinally, the FHMR also exhibits stable motion when subjected to the same external rotating field, as shown in Fig. 3L. Figure S11 presents a comparative analysis of the directional response of FHMRs with magnetic particles aligned along the long and short axes under an identical external magnetic field. This demonstrates that, through our fabrication method, FHMRs can select the appropriate nanoparticle alignment direction based on the requirements of different environments, enhancing the potential of FHMRs to perform multiple tasks.

Next, to validate the biocompatibility of FHMR, we conducted biocompatibility testing (fig. S12). In the culture environment containing FHMRs, the proliferation curve of A2780 human ovarian cancer cells over a 40-hour period showed no notable difference compared to the normal control group. Optical microscopy imaging and monitoring over 40 hours revealed that the cell morphology in the FHMR group was essentially consistent with that of the control group, with no noticeable signs of rupture, apoptosis, or necrosis observed, demonstrating that the cell proliferation capacity was not substantially affected. Moreover, to evaluate long-term coating stability in bioenvironments, we conducted 7-day of immersion tests (37°C) of long-axis and short-axis configuration FHMRs in simulated biofluids, including deionized water, gastric fluid (pH 1.2), fetal bovine serum (pH 7.4), and simulated intestinal fluid (pH 6.8). Key analyses included optical microscopy (fig. S13), grayscale contrast quantification (fig. S14), and the propulsion speed stability analysis (fig. S15). Results demonstrated the following: (i) No notable deformation has occurred in the FHMRs after 7 days immersion through time-dependent morphological monitoring. (ii) Grayscale analysis revealed no substantial increase in particle detachment. (iii) The frequency-velocity response error bar graph quantitatively confirms that the motility of FHMRs remains unaffected following prolonged exposure to biological or simulated biological fluids. These results validate the mechanical and chemical stability of FHMRs in complex biological environments.

Multimodal locomotion capability of FHMRs

To achieve multimodal locomotion of FHMRs, we used the OctoMag-like multidirectional magnetic control system, as shown in Fig. 1C, which can achieve decoupled control of magnetic forces and torques. By applying either a circular rotating magnetic field or a conical magnetic field to FHMR with different magnetization orientations, we were able to achieve various locomotion modes as shown in Fig. 4A: SFHR rolling mode, SFHR swing mode, SFHR rising mode, LFHR rotation mode, and LFHR swing mode. In 3D space, the rotating magnetic field $H_R(t)$ generated by the eight-coil magnetic control device can be represented by the following equation

$$H_{\mathrm{R}}(t) = H_0 R_x(\omega T) R_y(\omega T) R_z(\omega T) \tag{1}$$

where $R_x(\omega T)$, $R_y(\omega T)$, and $R_z(\omega T)$ are the rotation matrices around the x, y, and z axes, respectively. H_0 is the initial magnetic field vector. When a circular rotating magnetic field is applied in the yz plane, the above equation can be simplified to the following form

$$H_{\mathrm{R}}(t) = H_{\mathrm{R}}\left[\cos(\omega t)e_y - \sin(\omega t)e_z\right] \tag{2}$$

where ω represents angular velocity, H represents magnetic field intensity, and e represents a unit vector. As depicted in Fig. 4A, under this magnetic field, the LFHR exhibits rotation motion mode, while SFHR demonstrates rolling and rising motion modes. The conical rotating magnetic field applied to the FHMR is denoted as $H_W(t)$

$$H_W(t) = H_x e_x + H_W\left[\cos(\omega t)e_y - \sin(\omega t)e_z\right] \tag{3}$$

The notable variation in velocity between different modes is attributed to the mutual influence of the FHMR's motion state and the fluid's flow state. As shown in Fig. 4A, under this magnetic field, the LFHR and SFHR, respectively, show swing motion modes.

The motion state of the robot shows great differences in different motion modes (Fig. 4B). This is mainly due to the different

Downloaded from https://www.science.org at Koc Universitesi Suna Kirac on December 05, 2025

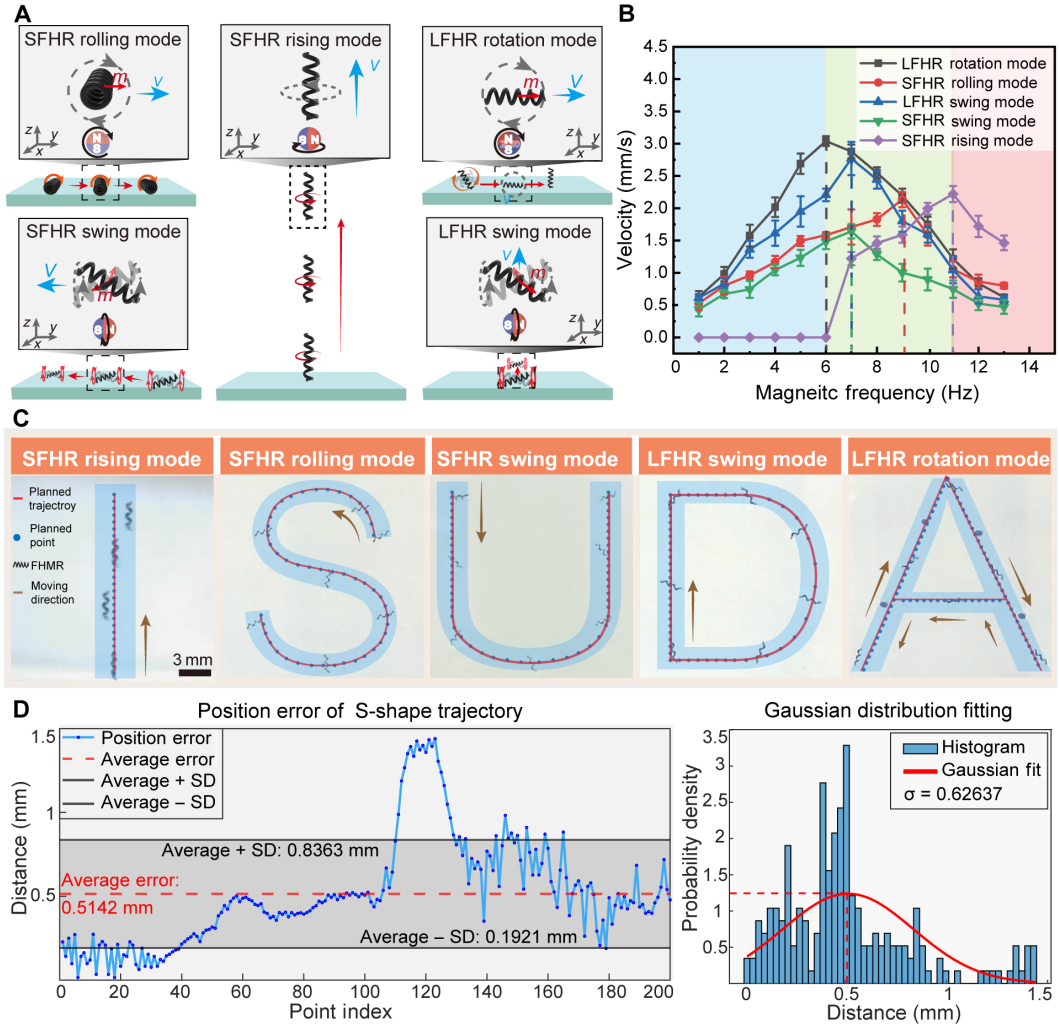


Fig. 4. FHMR five locomotion modes and trajectories. (**A**) The motion state concept diagram of five modes of the SFHR and LFHR include the motion state concept diagram of SFHR rolling mode, the motion state concept diagram of SFHR swing mode, the motion state concept diagram of SFHR rising mode, the motion state concept diagram of LFHR rotation mode, and the motion state concept diagram of LFHR swing mode. N denotes the north pole of the external magnetic field during MFR motion, and S represents the south pole of the external magnetic field during MFR motion. (**B**) The variation of the moving speed of these five modes with the changing of electromagnetic field frequency. The blue part in the figure represents the lower frequency band, the green part represents the middle frequency band, the green part represents the middle frequency band, and the red part represents the higher frequency band. (**C**) Experimental tracking results of the English character "ISUDA" through five different motion modes in a closed-loop control manner. (**D**) Taking the S-shaped trajectory as an example, the trajectory position error result and Gaussian distribution fitting diagram of FHMR of the S-shape trajectory. The error bars in (B) are the SDs calculated from three experiments.

hydrodynamic resistance and torque that they receive. Here, we apply the theory of fluid-solid interaction (Supplementary Text 4) to analyze the interaction between the FHMR and the fluid field. The resistance force exerted by the fluid on the FHMR's boundary F and the rotational torque exerted by the fluid on the FHMR's surface T are described by the following equations (*55*, *56*)

$$\int_{\Omega_{f-s}} \sigma_f \cdot \mathbf{n} ds = \mathbf{F} \tag{4}$$

$$\int_{\Omega_{f-s}} \sigma_f \times (r_s - r_c) \cdot \mathbf{n} ds = \mathbf{T} \tag{5}$$

where $\mathbf{r_s}$ and $\mathbf{r_c}$ are the position vectors of the surface and the center of the FHMR, and ds is the surface differential element defined on the boundary surface. $\mathbf{n}$ is the outward normal vector on $\Omega_{f\text{-}s}$. The hydrodynamic resistance force $\mathbf{F}$ and torque $\mathbf{T}$ at the fluid-solid interface $\Omega_{f\text{-}s}$ are derived under laminar flow conditions. The fluid-structure interaction boundary conditions governing FHMR motion are defined by three critical constraints: (i) no-slip condition at the fluid-solid interface, where fluid velocity v matches the robot's surface velocity $\mathbf{d}$ ($\mathbf{v} = \mathbf{d}$); (ii) force equilibrium requiring equal and opposite forces at the interface; and (iii) stress continuity ensuring $\sigma_f \cdot \mathbf{n} = \sigma_s \cdot \mathbf{n}$ at the interface. These constraints operate under laminar flow [Reynolds number (Re) $\approx 0.82 \ll 2000$], where shear stress and static pressure dominate interactions, excluding turbulence-induced pressure fluctuations.

Downloaded from https://www.science.org at Koc Universitesi Suna Kirac on December 05, 2025

Based on the modeling analysis described above, it can be deduced that, in the LFHR rotation mode, the FHMR exhibits a larger contact area with the fluid field and the highest tangential velocity. This results in the greatest surface stress, consequently generating the maximum force **F**. Additionally, the maximum value of $\mathbf{r_s} - \mathbf{r_c}$ results in the highest torque **T**. This ultimately leads to the smallest cutoff frequency for this mode, as once exceeded, the substantial drag and torque cause the magnetic torque to become insufficient to maintain synchronization between the rotation frequency and the magnetic field frequency as proved in Fig. 4B. In contrast, in the SFHR rolling mode, the tangential velocity is the lowest, and $\mathbf{r_s} - \mathbf{r_c}$ is minimal, resulting in the smallest **T** and **F** and, thus, a higher cutoff frequency. In the LFHR and SFHR swing modes, the FHMR experiences **T** and **F** between the aforementioned extremes cases; hence, their cutoff frequencies also fall between the two (Fig. 4B). In the SFHR rising mode, **T** becomes the driving force for the upward motion of the FHMR. As the external magnetic field frequency increases, the larger **T**, the higher the ascent velocity of the FHMR. However, when the magnetic field frequency exceeds 11 Hz, the drag exerted by the fluid becomes too substantial, and the magnetic torque can no longer maintain synchronization between the FHMR's rotational frequency and the magnetic field frequency.

To further validate the multimodal locomotion capability of the FHMR, we applied different magnetic fields to control the FHMR in five different modes as it traversed a trajectory spelling out the letters "ISUDA". In the experiment, a vision-based closed-loop control strategy is used (fig. S16). The specific experimental trajectories are shown in Fig. 4C. During the trajectory control process, magnetic field parameters need to be adjusted according to the characteristics of the desired trajectory to achieve precise control. In the S-shaped trajectory motion, we use the SFHR rolling mode for control, and the trajectory error values are shown in Fig. 4D. Most of the errors are tightly concentrated around 0.5 mm, which is only a quarter of the SFHR long axis. The Gaussian curve distribution coefficient σ is equal to 0.62637. The larger error peak of the S-shaped trajectory is mainly due to the relatively wide rolling axis of the SFHR rolling mode, which results in poorer mechanical responsiveness, making it more challenging for the FHMR to change direction. Detailed data for the other trajectories can be found in the Supplementary Materials (figs. S17 to S20 and movie S4). These results demonstrate the FHMR's robust capability for precise multimodal locomotion under magnetic control.

Adaptability of each locomotion mode to different tasks

The versatile motion mode of the robot gives it flexible and complex motion ability and the ability to adapt to various tasks. Figure 5 illustrates the strong adaptability to different tasks of the three modes of SFHR and the two modes of LFHR.

LFHR rotation mode

In the LFHR rotation mode, FHMR can climb the stair-shaped structure. It can be seen that the height of the stair is higher than the length of the FHMR. The length of the FHMR is 3 mm, and the height of each stair is 5 mm. When the FHMR rolls to the step position, the top of the FHMR can come into contact with the step surface. When FHMR performs rotation motion, the contact point can generate remarkable frictional force. In this mode, the FHMR extends to the most distance at both ends, resulting in the maximum frictional force gradient and the most pronounced generation of lift force. Due to the control of the rotating magnetic field, FHMR can continuously alternate the two ends as fulcrums and climb over steps through rotation. Therefore, it can overcome obstacles of certain heights, traverse complex barriers, and adapt to uneven in-body environments. The visual representation of FHMR's motion is depicted in Fig. 5A and movie S5. The contrary experiment of the longer long-axis FHMR climbing shorter barriers can be found in fig. S21. Additionally, we used the LFHR rolling mode to execute trajectory movement on the surface of the bovine stomach. As illustrated in fig. S22 and movie S6, although the predefined path was obstructed by obstacles, FHMR has strong flexibility due to the point contact with the bovine stomach surface in this mode, so FHMR can effectively bypass these obstacles and reach the target point.

LFHR swing mode

In the human body, the presence of folded environments, such as the stomach, can lead to the entrapment of the FHMR, ultimately compromising task success rates. Moreover, in fluid environments, the interplay between folded structures and fluid viscosity exacerbates boundary layer effects, which substantially reduces the locomotion speed of FHMR (*57*). Therefore, it is critical to evaluate the capability of FHMR to cross a folded terrain. Figure 5B demonstrates the FHMR's ability to navigate through the gap wider than the FHMR short axis in a folded terrain setting. We selected the LFHR swing mode and externally applied a 7-Hz magnetic field using a magnetic actuation system. This choice was made because the LFHR swing increases the range of movement of the FHMR. Once one end swings across the slit, the conical magnetic field applied by the magnetic actuation device allows the FHMR to use that end as a pivot, enabling the entire robot to swing across the slit. Ultimately, the results show that FHMRs using the LFHR swing mode can stably traverse a plane with several 1.5 mm gaps, while the width of the FHMR's short axis is less than 0.5 mm. Additionally, we used the FHMR short-axis rolling mode as a comparison. As shown in fig. S23 and movie S7, the FHMR in the SFHR rolling mode was unable to traverse the slit of the same width. The results from the final verification experiments indicate that the LFHR swing mode of the FHMR can effectively adapt to this environment.

SFHR swing mode

Due to the large distribution of small-diameter blood vessels required for regulating blood pressure and substance exchange in the human body, their flow velocity is often low, which also leads to the presence of impurities and blood clots. However, traditional microrobots are constrained by the limited movement space and high resistance within tiny blood vessels, which often restricts their movement in such environments. In SFHR swing mode, the FHMR can move inside curved and narrow pipelines because it can effectively contact the pipe wall, generating friction that enhances the robot's ability to move in narrow pipes, as shown in Fig. 5C. Additionally, the propulsive force generated by the robot is greater in SFHR swing mode, allowing it to penetrate a certain thickness of simulated thrombus, which made of lime powder. A conical rotating magnetic field drives the robot to oscillate and rotate along its longitudinal axis (movie S8).

SFHR rolling mode

Due to the low resistance to forward motion and stable movement characteristics of the FHMR in its SFHR rolling mode under a magnetic field, it can transport objects in highly confined environments. For instance, it can push a small ball to a predicted position through continuous impacts or contact, showcasing potential applications in confined and low-clearance environments, such as the removal of micro-impurities within joint capsules and joint cavities. The visual

Downloaded from https://www.science.org at Koc Universitesi Suna Kirac on December 05, 2025

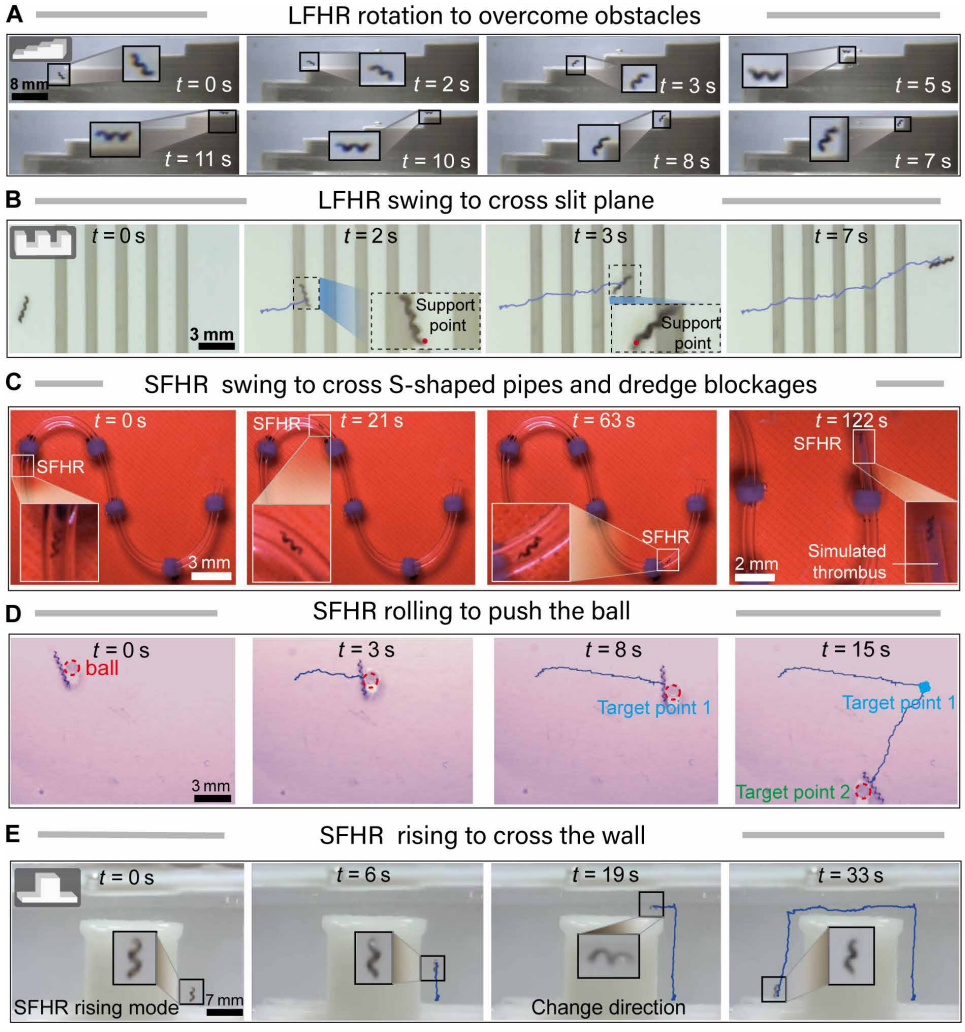


Fig. 5. Experimental demonstrations of the FHMR. (**A**) The moving process of FHMR overcoming obstacles in LFHR rolling mode. The subfigures are the magnified view of the FHMR as it traverses a step-like obstacle, providing a detailed depiction of its motion state. The subplot in the top left corner demonstrates the stepped structural configuration designed for this experiment. (**B**) Experimental image of LFHR swing mode crossing folded terrain. The subfigure is the magnified view of the FHMR as it passes through a gap, showing its state in detail when using one end as a pivot to cross the gap. The blue line represents the real trajectory. The subplot in the top left corner characterizes the multi-gap structural architecture. (**C**) Under the SFHR swing mode, clearing the simulated thrombus and moving through an S-shaped tube. The subfigures provide detailed view of the motion state of the FHMR inside the pipeline. (**D**) Pushing the ball of the FHMR in the SFHR rolling mode. The blue line represents the real trajectory. (**E**) FHMR crosses the wall in SFHR rising mode. The subfigures illustrate the motion state of the FHMR during ascent. The blue line represents the real trajectory. The subplot in the top left corner illustrates the boss-shaped structural model used in this experiment.

representation of FHMR's motion is shown in Fig. 5D and movie S9. Furthermore, the FHMR demonstrates relatively stable operation in high-density, low-curvature wrinkled environments through the SFHR rolling mode, as illustrated in fig. S24 and movie S10. Additionally, experimental results further demonstrate that the SFHR rolling mode can effectively adapt to environments with varying simulated vascular diameters (fig. S25 and movie S11). Clearly, across segments with different diameters, the FHMR can navigate in the environment with specific inclines. By dynamically adjusting the magnetic field direction in response to changes in the simulated vascular diameter, the FHMR leverages its exceptional motion stability in the SFHR rolling mode to traverse the conduit seamlessly.

SFHR rising mode

In a viscous environment such as blood plasma, 3D motion can be achieved using this model. The FHMR can climb across the wall of 20 mm, as shown in Fig. 5E and movie S12. The robot can be raised by applying the 10-Hz electromagnetic field in a solution with a dynamic viscosity of ~5 mPa·s. Upon reaching the target height, due to the considerable thickness of the wall, we opted to transform the horizontal rotation magnetic field to one perpendicular to the horizontal plane while maintaining a frequency of 10 Hz. This change redirected the FHMR's motion to horizontal movement. As the FHMR prepares to descend, we chose to reverse the current direction, thereby changing the rotation of the magnetic field from clockwise to counterclockwise

Downloaded from https://www.science.org at Koc Universitesi Suna Kirac on December 05, 2025

while still maintaining the 10-Hz magnetic field frequency, enabling controlled descent and precise arrival at the target location.

Combined multimodal control and application in complex environments

In Fig. 5C, we validated that the SFHR swing mode can traverse and clear blockages in narrow pipes. On the basis of this, we further assessed the motion capabilities of the SFHR in 3D complex terrains. We experimentally validated the motion of FHMR in a simulated complex human blood vessel environment by combining multiple modes of SFHR, as shown in Fig. 6A. The structure of the blood vessel is complex, featuring vertical channels, bends, and slopes. The FHMR can rise alone in the vertical vessel part in SFHR rising mode with a 10-Hz circular rotating electromagnetic field (Fig. 6B). As the FHMR ascended to the curved section of the vessel, there remained a certain distance to the slope section. Therefore, we switched to the SFHR swing mode, leveraging the precession effect generated by the swing to facilitate a smooth transition to the slope section. At 9 s, the FHMR reaches the slope part. The applied 5-Hz electromagnetic field is changing the mode to SFHR rolling mode. In the second curved section, we strategically used the SFHR swing mode as a transition, allowing the FHMR to switch more stably from the SFHR rolling mode to the short-axis ascent. At 29 s, we also apply the SFHR rising mode with a 10-Hz circular rotating electromagnetic field to the FHMR, which can make the robot successfully reach the target point through vertical 3D vessels (movie S13). This experiment demonstrates the characteristics of FHMR in controllable 3D motion. Based on the simulated thrombus removal experiment presented in Fig. 5C, combined with the validation of 3D vascular navigation, the FHMR demonstrates substantial potential for effective thrombus removal within complex 3D blood vessel networks.

To further explore its biomedical applications, we investigated the FHMR's potential in targeted drug delivery within complex biological/simulated biological environments. Due to the robot's strong surface adhesion, the FHMR demonstrates excellent drug-carrying capability. A drug encapsulation rate of more than 60% (mass ratio) can be achieved through simple drug deposition. The specific drug deposition process is shown in fig. S26. Additionally, its flexible motion modes make it highly suitable for targeted drug delivery in complex physiological environments, such as targeted drug delivery within the trachea in the lungs. The pulmonary environment contains a small amount of mucus, and its surface structure is highly complex, featuring countless tiny cilia. This presents a notable technical barrier for microrobots with single-mode locomotion in targeted drug delivery within the lungs. For microrobots with a single mode of motion, these factors present substantial technical barriers to targeted drug delivery in the lungs. Therefore, we developed an FHMR differential control strategy for targeted drug delivery. On the one hand, we used the larger stride length and lower rotational frequency of the LFHR rolling mode to enable FHMR to quickly reach the target site with minimal drug leakage. On the other hand, we used the higher swing frequency of the LFHR swing mode to facilitate drug release at the target site. Ultimately, this allowed targeted drug delivery within the complex and enclosed environment of the pulmonary bronchi, as shown in Fig. 6 (C and D). By applying a 4-Hz circular magnetic field, the FHMR is controlled to move to the target point through the LFHR rotation mode. The drug adsorbed on the FHMR can be released at the target point through the vibration of the FHMR under an 11-Hz conical magnetic field and switching to the LFHR swing mode (Fig. 6D and movie S14). In addition to targeted drug delivery, this differential control strategy is also applicable for removing harmful bacteria adhered to biological environments. Using an inner ear model as an example, under the rotation mode of the LFHR, the FHMR can move alone on the narrow pass. Under the LFHR swing mode, FHMR can generate stronger physical forces on the curved inner surface of biofilm plugs and tubes, making it easier for the robot to advance. As shown in fig. S27 and movie S15, we reached the target point and cleared the adhered simulated biofilm (yeast) by using the differential control strategy.

However, in certain highly corrosive in vivo environments (such as the stomach), methods based on drug deposition can result in drug loss, making efficient drug delivery difficult to achieve. To address this issue, a sustained-release coating strategy using PVA has been developed to mitigate drug dissolution loss in open drug-loading systems during transportation, with relevant validation experiments conducted in the gastric model and simulated gastric fluid as shown in Fig. 6E. Coating protection layer is formed on FHMRs through surface deposition of PVA solutions with varying ratios (water:PVA = 4:1 to 4:1.5) followed by thermal curing. The specific process of drug adsorption and coating protection layer encapsulation is shown in the fig. S28. By applying threshold segmentation to the original video results from static drug release comparison experiments involving uncoated FHMR and FHMR with varying coated protection thicknesses, validation data such as Fig. 6F and movie S16 are obtained. As shown in the Fig. 6F, the uncoated group lost 30% of the drug within ~9 min, whereas coated FHMRs required over 25 min to reach the same level of drug loss. Quantitative analysis further revealed tunable release profiles for coated FHMRs, with sustained-release efficacy dependent on the PVA-to-water ratio. Higher PVA concentrations yielded more pronounced sustained-release effects, as demonstrated by the 4:1.5 PVA-to-water ratio group, which exhibited the most substantial retardation in drug release. The optical image shown in Fig. 6G and movie S16 further demonstrates that the drug release from FHMRs coated with PVA at different concentrations was substantially reduced compared to uncoated FHMRs at the 20-min time point. The experimental data demonstrate that water-soluble PVA sustained-release coatings effectively mitigate drug dissolution losses during transport, while PVA concentration modulation enables temporal control over drug release kinetics. The experiment validated the entire transport-release process based on the differential control strategy as shown in Fig. 6H and movie S17: After FHMR quickly reaches the target through the LFHR rotation mode, it first remains stationary to allow the coating to dissolve and then switches to the LFHR swinging mode to accelerate the dissolution of the PVA coating and drug release. Quantitative evaluation of the gastric model shows that the drug release process can be decoupled into four characteristic stages (Fig. 6I): (1) static sustained release phase (baseline release rate) without external magnetic field influence and (2) micro-swing–induced release acceleration phase under a 3-Hz low-frequency conical magnetic field; (3) high-frequency swing-driven rapid release phase under an 11-Hz conical magnetic field; and (4) large-amplitude motion promoting drug diffusion phase using a circular rotating magnetic field. The slope changes of the release curves in each stage indicate that, compared to the baseline value in the first stage, the release rates in stages 2 to 4 are substantially enhanced, fully validating the dynamic enhancement effect of the differential control strategy on drug release efficiency. As shown in fig. S29, optical images further confirm this conclusion. Data analysis and experimental validation

Downloaded from https://www.science.org at Koc Universitesi Suna Kirac on December 05, 2025

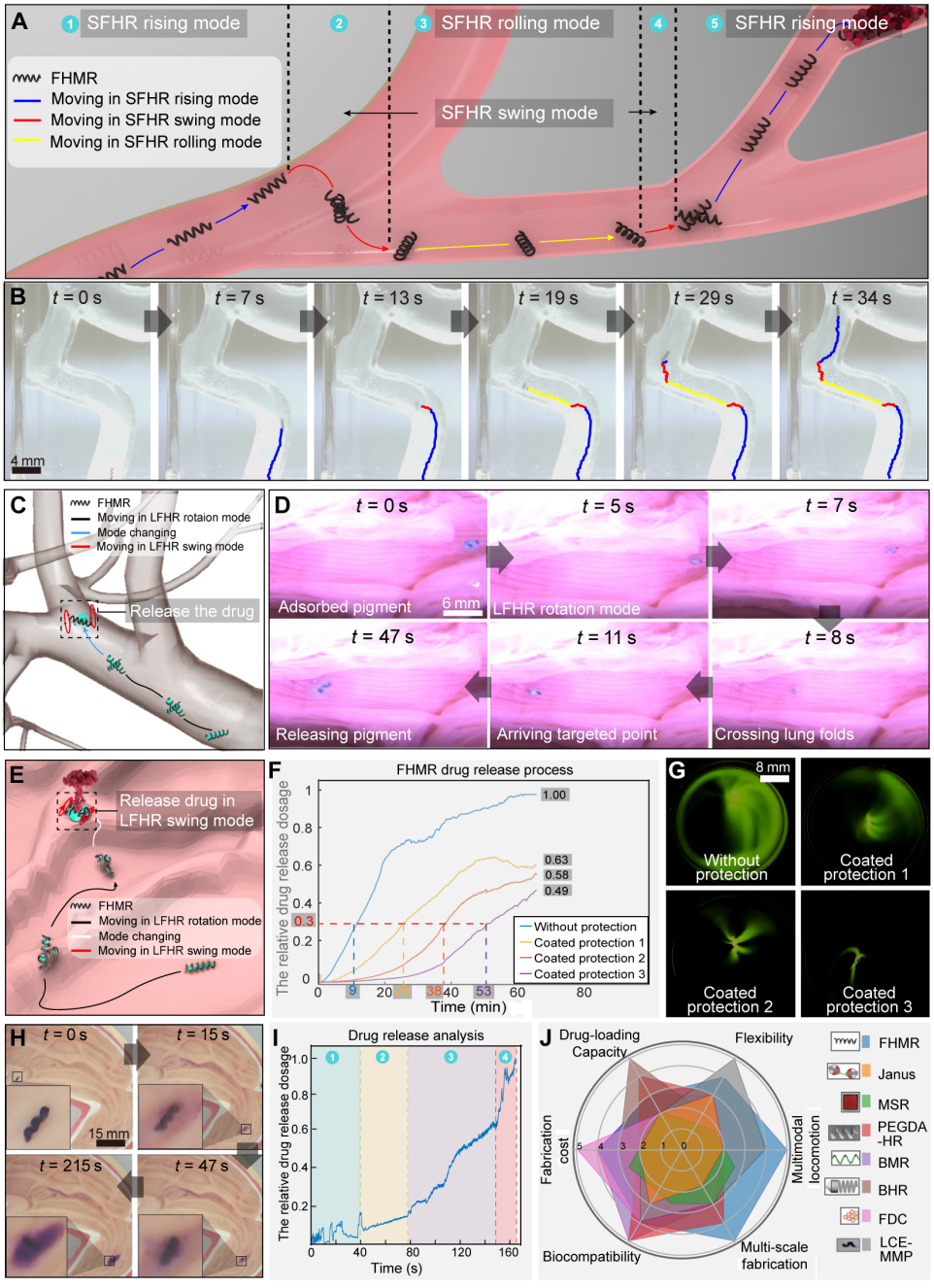


Fig. 6. Multimodal combined locomotion experiments of the FHMR. (**A**) Conceptual schematic illustrating the combined control of SFHR rising, swing and rotation modes, demonstrating its ability to navigate a 3D simulated blood vessel. (**B**) The specific motion process of SFHR during the verification experiment in a 3D simulated blood vessel. (**C**) Conceptual schematic of the LFHR demonstrating combined rolling and swinging motion control for targeted drug delivery in a pulmonary environment. (**D**) Sequential motion process of LFHR during the verification experiment in an ex vivo porcine lung. (**E**) Schematic illustrating the gastric administration process of FHMR with coated protection. (**F**) Relative drug release area and time-course curves comparing uncoated FHMR and coated variants with different layer thicknesses. The release area of the uncoated FHMR is normalized to 1. Coating variants 1, 2, and 3 are fabricated using water to PVA solution ratios of 4:1, 4:1.25, and 4:1.5, respectively, followed by heated air-drying. (**G**) Optical analysis of drug release after 20 min, comparing uncoated and coated FHMRs with different protection thicknesses. Images are obtained by subtracting the initial frame from subsequent frames in the original video. (**H**) Targeted drug delivery validation experiment of FHMR with coated protection in a gastric model. (**I**) The quantitative analysis of the drug release process in the stomach. Stage 1, 2, 3, and 4 are the static sustained release, the micro-swing–induced release acceleration, the high-frequency swing-driven rapid release, and the large-amplitude motion-enhanced diffusion, respectively. (**J**) Comparative analysis of FHMR and other magnetic helical robots, including BHR (*48*), LCE-MMP (*58*), Janus robot (*59*), PEDGA-HR (*39*), BMR (*26*), MSR (*60*), and FDC (*61*), based on multimodal locomotion, flexibility, drug-loading capacity, fabrication cost, biocompatibility, and multi-scale fabrication.

Downloaded from https://www.science.org at Koc Universitesi Suna Kirac on December 05, 2025

confirmed that the water-soluble PVA sustained-release coating effectively mitigated drug loss during transport. Moreover, by modulating PVA concentrations and FHMR locomotion modes, spatiotemporal control over drug release was achieved. This strategy provides experimental evidence for enhancing the biomedical applicability of magnetic control targeted drug delivery systems.

DISCUSSION

Inspired by the mechanics of machining swarf formation, this study presents a simple method for fabricating FHMRs on PMMA substrates via curved needle tip scribing. By using a multi-degree-of-freedom fabrication platform, various needle sizes, a compression-thermal fixation strategy, and different materials, the substrate, geometric structure, and dimensions of FHMRs can be adjusted from microns to millimeters. This fabrication method enables cost-effective and customizable manufacturing of FHMRs. Subsequent ferrofluid reconsolidation and dissolution processes allow the preparation of FHMRs with selectable long-axis or short-axis nanoparticle configurations. Under the control of an external magnetic field, these FHMRs activate five distinct motion modes in circular/conical rotating fields. Integrated mode-switching further validates FHMRs' navigability and capability of foreign matter removal in simulated biological environments, while a differential control strategy coupled with a sustained-release coating based on water-soluble PVA demonstrates the feasibility of targeted drug delivery in complex environments.

Experimental results demonstrate that FHMRs exhibit substantial advantages over other microrobots in targeted therapy applications. Building on this work, we benchmark FHMRs against existing microrobots across six dimensions, as shown in Fig. 6J and fig. S30. FHMRs exhibit five motion modes, surpassing the robot based on liquid crystal elastomer film embeded with magnetic micro-particles (LCE-MMP) (*58*) (three modes) and Janus/multilayer soft robots (*59*). This multimodal locomotion ability arises from the adjustable geometric arrangement of the nanoparticles. FHMRs also demonstrate remarkable flexibility. With the LFHR point-contact mechanism, FHMRs can achieve a maximum speed of 3 mm/s, outperforming polyethylene glycol diacrylate based helical robot (PEGDA-HR) (*39*) and biohybrid magnetic robot (BMR) (*26*) (<0.3 mm/s). Rapid directional adjustments enhance obstacle avoidance and targeting accuracy. In terms of biocompatibility, FHMRs show competitive advantages. Compared to NdFeB-based multi-layer soft robot (MSR) (*60*), which exhibits some electrochemical corrosion, PEGDA-HR (*39*) (hydrolytic degradation) and BMR (*26*) (spirulina biodegradability) offer stronger biocompatibility due to the characteristics of their fabrication materials. However, FHMRs excel in multi-scale fabrication, offering notable advantages. The fabrication method supports multi-scale production (from microns to millimeters), addressing the limitations of TPL-based PEGDA-HR (*39*) in large-scale manufacturing and the size constraints of BMR (*60*) from microbial templates. Additionally, FHMRs feature a lower complexity fabrication process and extremely low production costs, avoiding the high costs, complex manufacturing processes, and limited material compatibility associated with direct laser writing and TPL. Regarding drug-loading capacity, biomimetic helical robot (BHR) (*48*) and PEGDA-HR demonstrate superior performance in payload capacity and encapsulation stability. In contrast, ferrofluid droplet collectives (FDC) (*61*) is constrained by its material's low stiffness, resulting in limited drug-loading capability. Comparatively, FHMRs strike a superior balance between adaptability and cost-effectiveness. As evident from the radar chart (Fig. 6J), FHMRs achieve balanced performance across all dimensions, with particular strengths in multimodal locomotion, multi-scale fabrication, and low cost. Consequently, FHMRs demonstrate strong competitiveness for targeted therapy in the complex 3D environments of the human body. For a more detailed comparison and explanation, please refer to Supplementary Text S5.

The customizable and reconfigurable design of FHMR shows potential for tasks like targeted drug delivery and clearing obstructions in various human systems (e.g., urinary tract, bile ducts, and vascular systems) (*62*). However, the impact of marked in vivo environmental changes on its motion performance needs further study. For example, variations in blood pressure and vessel diameters affect fluid shear forces, influencing FHMR movement (*63*). Now, FHMR control relies on the non-intelligent selection of motion modes and experimental validation. Future work could incorporate machine learning to integrate tissue and fluid characteristics for autonomous mode selection and control. While this study used visual feedback with a charge-coupled device (CCD) camera, clinical use would require fluoroscopic imaging. FHMR's visibility under x-ray could be enhanced by increasing the volume of radiopaque particles, a focus for future research to expand its medical applications (*64*). In addition, due to the limitations of commercially available needles, the minimum resolution of the helical structures fabricated in this study is restricted. By using needles with finer diameters, smaller and more intricate helical structures can be produced. For instance, research related to nanoindentation has shown that spiral-like structures can accidentally form during the nanoscale indentation process, with these structures reaching sub-nanometer scales (*65*). Our prior research has confirmed that FHMRs are compatible with needles of varying diameters and a range of materials. Moving forward, we aim to develop robots with higher resolution and investigate the fabrication of diverse materials to address the challenges posed by complex and demanding physiological environments.

MATERIALS AND METHODS

Modeling of the magnetic field and forces

Magnetic field model

On the one hand, compared with FHMR, the electromagnetic coil size of the OctoMag-like magnetic control system is much larger. On the other hand, the robot is also far away from the coil, and the coil is also wrapped around an iron core. Therefore, the magnetic field generated by the coil can be approximated as a magnetic dipole. The resultant magnetic field distribution, propagated by the dipole, is as follows (*66*)

$$\mathrm{B_e}\left(M_i;\mathbf{r}\right)=\frac{\mu_0}{4\pi}\left(\frac{3M_i\cdot\mathbf{r}}{\mathbf{r}^5}-\frac{M_i}{\mathbf{r}^3}\right) \tag{6}$$

where M_i represents the magnetization of the magnetic dipole, $\mathbf{r}$ represents the space distance vector, and μ_0 represents the vacuum magnetic permeability. Here, we modeled the magnetic field generated by their cored electromagnet by approximating it as a magnetic dipole aligned along its longitudinal axis. The equivalent magnetic dipole is then spatially positioned following the geometric configuration of the electromagnet.

Magnetic force and torque acting on FHMR

The force $\mathbf{F}$ and the torque $\mathbf{T}$ acting on FHMR in a magnetic field can be determined using the following equations (*67*)

Downloaded from https://www.science.org at Koc Universitesi Suna Kirac on December 05, 2025

$$\mathbf{F} = (\mathbf{m} \cdot \nabla)\mathbf{B} \tag{7}$$

$$\mathbf{T} = \mathbf{m} \times \mathbf{B} \tag{8}$$

where **m** represents the magnetic moment of a magnetic dipole, **B** represents the magnetic field, and ∇ denotes the Nabla operator. Taking the gradient of the magnetic field vector **B** results in a 3 × 3 magnetic field gradient tensor matrix **G**. Substituting this into Maxwell's equations and further decomposing Eqs. 7 and 8, the mapping relationship from the magnetic field direction and gradient to the force and torque experienced by the magnetic microrobot can be derived, as expressed in the following equations

$$\begin{bmatrix} \mathbf{F} \\ \mathbf{B} \end{bmatrix} = \begin{bmatrix} F_k(m) & 0 \\ 0 & E_{3\times3} \end{bmatrix} \mathbf{U} = \mathbf{W}(m)\mathbf{U} \tag{9}$$

where $\mathbf{W}_R$ (**m**) represents the mapping matrix from the magnetic field input vector to the force and torque experienced by the FHMR. **U** represents the magnetic field input vector in space

$$\mathbf{U} = \begin{bmatrix} \frac{\partial B_x}{\partial x} & \frac{\partial B_x}{\partial y} & \frac{\partial B_x}{\partial z} & \frac{\partial B_y}{\partial y} & \frac{\partial B_y}{\partial z} & B_x & B_y & B_z \end{bmatrix}^T \tag{10}$$

Control theory of the electromagnetic drive system and the magnetic field

In this study, the OctMag-like magnetic control system composed of eight distributed coil units is used to control the magnetic field input vector **U**. Furthermore, the external magnetic field can trigger multimodal motion by applying magnetic force and torque to the FHMR within the workspace.

Assuming that the electromagnetic coils exhibit no substantial hysteresis effects and that the magnetic field strength generated by each coil in the electromagnetic drive system's workspace is linearly related to the current passing through the coil, the mapping relationship from the current input vector to the magnetic field input vector can be expressed as (*68*)

$$\mathbf{U} = \begin{bmatrix} \mathbf{G}_{5\times1} \\ \mathbf{B}_{3\times1} \end{bmatrix} = \begin{bmatrix} \mathscr{G}(\mathbf{p}) \\ \mathscr{B}(\mathbf{p}) \end{bmatrix} \begin{bmatrix} i_1 \\ \vdots \\ i_N \end{bmatrix} = \mathbf{L}(p)\mathbf{I} \tag{11}$$

where **G(p)** and **B(p)** represent the unit magnetic field gradient and magnetic field strength matrices at position pin space, respectively. **G** and **B** are 5 × 8 and 3 × 8 matrices, respectively. The **L(p)** matrix is an 8 × 8 matrix that represents the mapping relationship from the current input vector **I** to the magnetic field input vector **U**.

In a spatial environment, the orientation of a freely suspended magnetic body will ultimately align with the direction of the magnetic field lines at its location, and the attitude of the microrobot can be controlled by manipulating the direction of the external magnetic field vector **B** itself. The relationship from the current to the force and torque experienced by the FHMR can be expressed as

$$\begin{bmatrix} \mathbf{F} \\ \mathbf{B} \end{bmatrix} = \mathbf{W}(\mathbf{m})\mathbf{L}(p)\mathbf{I} = \mathscr{A}_{F,B}(m,p)\mathbf{I} \tag{12}$$

where $\mathscr{A}_{F,B}(\mathbf{m}, \mathbf{p})$ represents the forward mapping relationship matrix between the input current vector and the force/pose of the FHMR at position **p** within the workspace. To drive the FHMR to achieve multimodal motion, the required driving current is computed after specifying the desired force and pose of the FHMR. The force and pose vector of the FHMR contains six elements, corresponding to a forward mapping matrix $\mathscr{A}_{F,B}(\mathbf{m}, \mathbf{p})$, which is a 6 × 8 matrix. Because this matrix cannot be directly inverted, the required inverse mapping can be obtained using the pseudo-inverse method

$$\mathbf{I} = \mathscr{A}^{\dagger}_{F,B}(m,p) \begin{bmatrix} F_{\text{desired}} \\ B_{\text{desired}} \end{bmatrix} \tag{13}$$

where $\mathscr{A}^{\dagger}_{F,B}(\mathbf{m}, \mathbf{p})$ represents the inverse mapping matrix of the electromagnetic drive unit model. $[\mathbf{F}_{\text{desired}}, \mathbf{B}_{\text{desired}}]^T$ denotes the desired force and desired pose, while the current vector **I** represents the required current input vector for the electromagnetic drive unit when the FHMR, located at position **p** with a magnetic moment **m**, experiences the desired force $\mathbf{F}_{\text{desired}}$ and aligns with the desired pose $\mathbf{B}_{\text{desired}}$.

Magnetic field measurement

In this study, we use a Hall sensor (TLE493D-W2B6, Infineon Technologies AG) to measure the magnetic field. This sensor is capable of detecting the magnetic field intensity in all three dimensions. The Hall sensor is integrated with a three-axis motion platform, enabling the measurement of the three magnetic field components (B_x, B_y, and B_z) generated by the electromagnetic coils. The output signals from the Hall sensor are acquired via a serial port. Additionally, a LabVIEW-based software application was developed to facilitate the traversal of the sensor to any point within the workspace, ensuring comprehensive field measurements.

Simulation model of FHMR fabrication process

To accurately simulate material cutting behavior, the Johnson-Cook material yield model and the Johnson-Cook material failure model were adopted. The expression of the Johnson-Cook material yield model is as follows (*69*)

$$\sigma = \left[A + B\left(\varepsilon^{pt}\right)^n\right]\left[1 + C\ln\left(\frac{\varepsilon^{pt}}{\varepsilon_0}\right)\right]\left(1 - \theta^m\right) \tag{14}$$

where *A*, *B*, *C*, *n*, and *m* are the five physical property constants of the Johnson-Cook material yield model. *A* is the initial yield stress, *B* is the hardening stress, *C* is the strain rate constant, *n* is the hardening index, and *m* is the thermal softening index. Among them, the five major material physical property constants of the workpiece material are *A* = 224 Pa, *B* = 426 Pa, *C* = 0.002, *n* = 0.2, and *m* = 0.859. The Johnson-Cook material failure model expression is as follows

$$\varepsilon_f = \left\{ D_1 + D_2 exp\left[D_3\left(\frac{\sigma_m}{\sigma_{eq}}\right)\right]\right\}[1 + D_4 \ln(\varepsilon_p^*)][1 + D_5 T^*] \tag{15}$$

where D_1, D_2, D_3, D_4, and D_5 are five failure parameters. Among them, D_1, D_2, and D_3 can be determined through quasi-static tensile and torsional tests on notched round rods at room temperature, D_4 can be determined through tensile tests on smooth round rods at different strain rates and Hopkinson dynamic compression tests at room temperature, and D_5 can be determined through quasi-static tensile tests on smooth round rods at different temperatures. Among them, the D_1 of the workpiece material is 0.0261, D_2 = 0.263,

Downloaded from https://www.science.org at Koc Universitesi Suna Kirac on December 05, 2025

$D_3 = 0.349$, $D_4 = 0.247$, and $D_5 = 16.8$. The failure displacement of the material is $1e^{-5}$.

Motion control strategy of FHMR

In addition to the open-loop control method based on a joystick, we also implemented a proportional-integral-derivative control strategy as a closed-loop approach to enable the FHMR to move along a predetermined trajectory (fig. S6). The mathematical expression for this is as follows

$$u(t) = K_p e(t) + K_i \int_0^t e(t)\,dt + K_d \frac{de(t)}{dt} \quad (16)$$

where K_p is the proportional gain, K_i is the integral gain, K_d is the differential gain, and $e(t)$ is the error value at t time. Our control strategy is implemented using LabVIEW, where input parameters such as magnetic field frequency and steering angle are calculated on the basis of the difference between the actual position and the reference position.

Experimental setup and systems

The computer as the host of the magnetic control system is used to display the interactive interface and perform data visualization; a DAQ board (Smacq-3110) was used to output and transmit the desired control signals in an addressable manner. Eight power amplifiers were used to amplify the signals before connecting with the coils. The broad view field above the device allowed the installation of an upright microscope to obtain the position and potential orientation information of the FHMR, with the resolution of the installed CCD camera being 1600 × 1200 pixels. The control module, having an Intel Core i7 3.0-GHz processor, was used to run the LabVIEW-based customized software that includes real-time imaging tracking programs and control algorithms, which enables the magnetic control system to output preprogrammed control signals or receive remote control signals from a joystick to guarantee the dexterity of the magnetic control system.

Fabrication of the experimental test structures

The simulated blood vessel, convex platform, obstacles, simulated ear, and small balls used in the experiments listed in this article are all fabricated with a photo curable 3D printer (ELEGOO Saturn 3 Ultra). White and transparent water-washable ABS-like resin served as the printing material. All the structures used in the paper are cleaned by a vacuum plasma cleaner (PDC-MG, MING HENG) to ensure a smooth surface and prevent FHMR from sticking to the surface. The experimental structure used in the targeted drug delivery in the pulmonary environment is a real pig lung. In the 3D motion wall-climbing and vascular crossing experiments, we added glycerol to simulate an in vivo viscous environment with a water-to-glycerol ratio of 1:1, resulting in a solution dynamic viscosity of about 5 mPa·s, which is comparable to the viscosity of blood.

Supplementary Materials

The PDF file includes:

Supplementary Notes S1 to S3
Figs. S1 to S30
Tables S1 and S2
Supplementary Texts S1 to S5
Legends for movies S1 to S17

Other Supplementary Material for this manuscript includes the following:

Movies S1 to S17

REFERENCES AND NOTES

1. F. Soto, J. Wang, R. Ahmed, U. Demirci, Medical micro/nanorobots in precision medicine. *Adv. Sci.* **7**, 2002203 (2020).
2. H. Ceylan, N. O. Dogan, I. C. Yasa, M. N. Musaoglu, Z. U. Kulali, M. Sitti, 3D printed personalized magnetic micromachines from patient blood-derived biomaterials. *Sci. Adv.* **7**, eabh0273 (2021).
3. Y. Dong, L. Wang, N. Xia, Z. Yang, C. Zhang, C. Pan, D. Jin, J. Zhang, C. Majidi, L. Zhang, Untethered small-scale magnetic soft robot with programmable magnetization and integrated multifunctional modules. *Sci. Adv.* **8**, eabn8932 (2022).
4. B. J. Nelson, S. Gervasoni, P. W. Y. Chiu, L. Zhang, A. Zemmar, Magnetically actuated medical robots: An in vivo perspective. *Proc. IEEE* **110**, 1028–1037 (2022).
5. C. K. Schmidt, M. M. Sánchez, R. J. Edmondson, O. G. Schmidt, Engineering microrobots for targeted cancer therapies from a medical perspective. *Nat. Commun.* **11**, 5618 (2020).
6. S. Jeon, S. Kim, S. Ha, S. Lee, E. Kim, S. Y. Kim, S. H. Park, J. H. Jeon, S. W. Kim, C. Moon, B. J. Nelson, J.-Y. Kim, S.-W. Yu, H. Choi, Magnetically actuated microrobots as a platform for stem cell transplantation. *Sci. Robot.* **4**, eaav4317 (2019).
7. X. Fan, Y. Zhang, Z. Wu, H. Xie, L. Sun, T. Chen, Z. Yang, Combined three dimensional locomotion and deformation of functional ferrofluidic robots. *Nanoscale* **15**, 19499–19513 (2023).
8. I. S. Khalil, A. F. Tabak, K. Sadek, D. Mahdy, N. Hamdi, M. Sitti, Rubbing against blood clots using helical robots: Modeling and in vitro experimental validation. *IEEE Robot. Autom. Lett.* **2**, 927–934 (2017).
9. X. Fan, Q. Hu, L. Sun, H. Xie, H. Sun, Z. Yang, Large-scale swarm control of microrobots by a hybrid-style magnetic actuation system. *IEEE Trans. Ind. Electron.* **71**, 10998–11008 (2024).
10. D. Son, H. Gilbert, M. Sitti, Magnetically actuated soft capsule endoscope for fine-needle biopsy. *Soft Robot.* **7**, 10–21 (2020).
11. F. Qiu, S. Fujita, R. Mhanna, L. Zhang, B. R. Simona, B. J. Nelson, Magnetic helical microswimmers functionalized with lipoplexes for targeted gene delivery. *Adv. Funct. Mater.* **25**, 1666–1671 (2015).
12. W. Lee, S. Jeon, J. Nam, G. Jang, Dual-body magnetic helical robot for drilling and cargo delivery in human blood vessels. *J. Appl. Phys.* **117**, 17B314 (2015).
13. I. C. Yasa, H. Ceylan, U. Bozuyuk, A.-M. Wild, M. Sitti, Elucidating the interaction dynamics between microswimmer body and immune system for medical microrobots. *Sci. Robot.* **5**, eaaz3867 (2020).
14. F. Qiu, B. J. Nelson, Magnetic helical micro-and nanorobots: Toward their biomedical applications. *Engineering* **1**, 021–026 (2015).
15. V. Magdanz, M. Medina-Sánchez, L. Schwarz, H. Xu, J. Elgeti, O. G. Schmidt, Spermatozoa as functional components of robotic microswimmers. *Adv. Mater.* **29**, 1606301 (2017).
16. F. Mou, Y. Li, C. Chen, W. Li, Y. Yin, H. Ma, J. Guan, Single-component TiO_2 tubular microengines with motion controlled by light-induced bubbles. *Small* **11**, 2564–2570 (2015).
17. Q. Li, H. Chen, X. Feng, C. Yu, F. Feng, Y. Chai, P. Lu, T. Song, X. Wang, L. Yao, Nanoparticle-regulated semiartificial magnetotactic bacteria with tunable magnetic moment and magnetic sensitivity. *Small* **15**, 1900427 (2019).
18. K. E. Peyer, S. Tottori, F. Qiu, L. Zhang, B. J. Nelson, Magnetic helical micromachines. *Chemistry* **19**, 28–38 (2013).
19. D. Zhong, W. Li, Y. Qi, J. He, M. Zhou, Photosynthetic biohybrid nanoswimmers system to alleviate tumor hypoxia for FL/PA/MR imaging-guided enhanced radio-photodynamic synergetic therapy. *Adv. Funct. Mater.* **30**, 1910395 (2020).
20. B. J. Nelson, I. K. Kaliakatsos, J. J. Abbott, Microrobots for minimally invasive medicine. *Annu. Rev. Biomed. Eng.* **12**, 55–85 (2010).
21. M. Sitti, Miniature soft robots-Road to the clinic. *Nat. Rev. Mater.* **3**, 74–75 (2018).
22. D. Son, M. C. Ugurlu, M. Sitti, Permanent magnet array–driven navigation of wireless millirobots inside soft tissues. *Sci. Adv.* **7**, eabi8932 (2021).
23. W. Hu, G. Z. Lum, M. Mastrangeli, M. Sitti, Small-scale soft-bodied robot with multimodal locomotion. *Nature* **554**, 81–85 (2018).
24. F. Qiu, L. Zhang, K. E. Peyer, M. Casarosa, A. Franco-Obregón, H. Choi, B. J. Nelson, Noncytotoxic artificial bacterial flagella fabricated from biocompatible ORMOCOMP and iron coating. *J. Mater. Chem. B* **2**, 357–362 (2014).
25. P. L. Venugopalan, R. Sai, Y. Chandorkar, B. Basu, S. Shivashankar, A. Ghosh, Conformal cytocompatible ferrite coatings facilitate the realization of a nanovoyager in human blood. *Nano Lett.* **14**, 1968–1975 (2014).
26. X. Yan, Q. Zhou, M. Vincent, Y. Deng, J. Yu, J. Xu, T. Xu, T. Tang, L. Bian, Y.-X. J. Wang, K. Kostarelos, L. Zhang, Multifunctional biohybrid magnetite microrobots for imaging-guided therapy. *Sci. Robot.* **2**, eaaq1155 (2017).
27. F. Zhang, Z. Guo, Z. Li, H. Luan, Y. Yu, A. T. Zhu, S. Ding, W. Gao, R. H. Fang, L. Zhang, J. Wang, Biohybrid microrobots locally and actively deliver drug-loaded nanoparticles to inhibit the progression of lung metastasis. *Sci. Adv.* **10**, eadn6157 (2024).

Downloaded from https://www.science.org at Koc Universitesi Suna Kirac on December 05, 2025

28. C. Chen, S. Ding, J. Wang, Materials consideration for the design, fabrication and operation of microscale robots. *Nat. Rev. Mater.* **9**, 159–172 (2024).
29. L.-L. Ma, C. Liu, S.-B. Wu, P. Chen, Q.-M. Chen, J.-X. Qian, S.-J. Ge, Y.-H. Wu, W. Hu, Y.-Q. Lu, Programmable self-propelling actuators enabled by a dynamic helical medium. *Sci. Adv.* **7**, eabh3505 (2021).
30. K. Kamata, S. Suzuki, M. Ohtsuka, M. Nakagawa, T. Iyoda, and, A. Yamada, Fabrication of left-handed metal microcoil from spiral vessel of vascular plant. *Adv. Mater.* **23**, 5509–5513 (2011).
31. F. Zhang, Z. Li, Y. Duan, A. Abbas, R. Mundaca-Uribe, L. Yin, H. Luan, W. Gao, R. H. Fang, L. Zhang, J. Wang, Gastrointestinal tract drug delivery using algae motors embedded in a degradable capsule. *Sci. Robot.* **7**, eabo4160 (2022).
32. N. Billinton, A. W. Knight, Seeing the wood through the trees: A review of techniques for distinguishing green fluorescent protein from endogenous autofluorescence. *Anal. Biochem.* **291**, 175–197 (2001).
33. K. Kamata, Z. Piao, S. Suzuki, T. Fujimori, W. Tajiri, K. Nagai, T. Iyoda, A. Yamada, T. Hayakawa, M. Ishiwara, S. Horaguchi, A. Belay, T. Tanaka, K. Takano, M. Hangyo, Spirulina-templated metal microcoils with controlled helical structures for THz electromagnetic responses. *Sci. Rep.* **4**, 4919 (2014).
34. A. Ramos-Sebastian, J. S. Lee, S. H. Kim, Multimodal locomotion of magnetic droplet robots using orthogonal pairs of coils. *Adv. Intell. Syst.* **5**, 2300133 (2023).
35. X. Li, F. Zhao, W. Rong, D. Li, H. Xie, A mucoadhesive magnetic millimeter-scale robot with two motion modes for drug delivery to the colon. *Appl. Mater. Today* **35**, 101941 (2023).
36. R. Dreyfus, Q. Boehler, S. Lyttle, P. Gruber, J. Lussi, C. Chautems, S. Gervasoni, J. Berberat, D. Seibold, N. Ochsenbein-Kölble, M. Reinehr, M. Weisskopf, L. Remonda, B. J. Nelson, Dexterous helical magnetic robot for improved endovascular access. *Sci. Robot.* **9**, eadh0298 (2024).
37. Y. Sun, R. Pan, Y. Chen, Y. Wang, L. Sun, N. Wang, X. Ma, G. P. Wang, Efficient preparation of a magnetic helical carbon nanomotor for targeted anticancer drug delivery. *ACS Nanosci. Au*, **1**, 3, 94–102 (2022).
38. Y. Dong, L. Wang, Z. Zhang, F. Ji, T. K. F. Chan, H. Yang, C. P. L. Chan, Z. Yang, Z. Chen, W. T. Chang, J. Y. K. Chan, J. J. Y. Sung, L. Zhang, Endoscope-assisted magnetic helical micro- machine delivery for biofilm eradication in tympanostomy tube. *Sci. Adv.* **8**, eabq8573 (2022).
39. H. Lee, D. Kim, S. Kwon, S. Park, Magnetically actuated drug delivery helical microrobot with magnetic nanoparticle retrieval ability. *ACS Appl. Mater. Interfaces*, **13**, 17, 19633–19647 (2021).
40. J. P. Desai, *Encyclopedia Of Medical Robotics* (World Scientific Press, 2018).
41. X. Chen, C. Tian, H. Zhang, H. Xie, Biodegradable magnetic hydrogel robot with multi-modal locomotion for targeted cargo delivery. *ACS Appl. Mater. Interfaces*, **15**, 24, 28922–28932 (2023).
42. M. B. Akolpoglu, Y. Alapan, N. O. Dogan, S. F. Baltaci, O. Yasa, G. A. Tural, M. Sitti, Magnetically steerable bacterial microrobots moving in 3D biological matrices for stimuli-responsive cargo delivery. *Sci. Adv.* **8**, eabo6163 (2022).
43. W. Chen, X. Chen, M. Yang, S. Li, X. Fan, H. Zhang, H. Xie, Triple-configurational magnetic robot for targeted drug delivery and sustained release. *ACS Appl. Mater. Interfaces* **13**, 45315–45324 (2021).
44. Z. Ye, Y. Wang, S. Liu, D. Xu, W. Wang, X. Ma, Construction of nanomotors with replaceable engines by supramolecular machine-based host-guest assembly and disassembly. *J. Am. Chem. Soc.* **143**, 15063–15072 (2021).
45. B. Wang, K. F. Chan, K. Yuan, Q. Wang, X. Xia, L. Yang, H. Ko, Y.-X. J. Wang, J. J. Y. Sung, P. W. Y. Chiu, L. Zhang, Endoscopy-assisted magnetic navigation of biohybrid soft microrobots with rapid endoluminal delivery and imaging. *Sci. Robot.* **6**, eabd2813 (2021).
46. Y. Dong, L. Wang, K. Yuan, F. Ji, J. Gao, Z. Zhang, X. Du, Y. Tian, Q. Wang, L. Zhang, Magnetic microswarm composed of porous nanocatalysts for targeted elimination of biofilm occlusion. *ACS Nano* **15**, 5056–5067 (2021).
47. M. P. Kummer, J. J. Abbott, B. E. Kratochvil, R. Borer, A. Sengul, B. J. Nelson, OctoMag: An electromagnetic system for 5-DOF wireless micromanipulation. *IEEE Trans. Robot.* **26**, 1006–1017 (2010).
48. Z. Wang, Q. Li, P. Cao, J. Zhang, D. Wu, R. Xu, Y. Zhang, Y. Xu, T. Liang, W. Chen, L. Wang, X. Chen, A biomimetic helical robot actuated by rotating magnetic field for targeted navigation and in situ prodrug activation to treat intestinal diseases. *Device* **1**, 100064 (2023).
49. H. Zhang, B. Xu, Y. Ouyang, Y. Wang, H. Zhu, G. Huang, J. Cui, Y. Mei, Shape memory alloy helical microrobots with transformable capability towards vascular occlusion treatment. *Research* **2022**, 9842752 (2022).
50. M. Sun, B. Hao, S. Yang, X. Wang, C. Majidi, L. Zhang, Exploiting ferrofluidic wetting for miniature soft machines. *Nat. Commun.* **13**, 7919 (2022).
51. R. Deb, B. Sarma, A. Dalal, Magnetowetting dynamics of sessile ferrofluid droplets: A review. *Soft Matter* **18**, 2287–2324 (2022).
52. J. Kim, S. E. Chung, S. E. Choi, H. Lee, J. Kim, S. Kwon, Programming magnetic anisotropy in polymeric microactuators. *Nat. Mater.* **10**, 747–752 (2011).
53. V. Cabuil, N. Hochart, R. Perzynski, P. J. Lutz, Synthesis of cyclohexane magnetic fluids through adsorption of end-functionalized polymers on magnetic particles. *Trends Colloid Interface Sci. VIII* **97**, 71–74 (1994).
54. X. Yang, W. Shang, H. Lu, Y. Liu, L. Yang, R. Tan, X. Wu, Y. Shen, An agglutinate magnetic spray transforms inanimate objects into millirobots for biomedical applications. *Sci. Robot.* **5**, eabc8191 (2020).
55. P. S. Bernard, *Fluid Dynamics* (Cambridge Univ. Press, 2015).
56. N. Hu, L. Ding, A. Wang, W. Zhou, C. Zhang, B. Zhang, R. Yin, Comprehensive modeling of corkscrew motion in micro−/nano-robots with general helical structures. *Nat. Commun.* **15**, 7399 (2024).
57. H. K. Mofatt, Viscous and resistive eddies near a sharp corner. *J. Fluid Mech.* **18**, 1–18 (1964).
58. J. Zhang, Y. Guo, W. Hu, R. H. Soon, Z. S. Davidson, M. Sitti, Liquid crystal elastomer-based magnetic composite films for reconfigurable shape-morphing soft miniature machines. *Adv. Mater.* **33**, e2006191 (2021).
59. X. Hu, I. C. Yasa, Z. Ren, S. R. Goudu, H. Ceylan, W. Hu, M. Sitti, Magnetic soft micromachines made of linked microactuator networks. *Sci. Adv.* **7**, eabe8436 (2021).
60. Z. Chen, Y. Wang, H. Chen, J. Law, H. Pu, S. Xie, F. Duan, Y. Sun, N. Liu, J. Yu, A magnetic multi-layer soft robot for on-demand targeted adhesion. *Nat. Commun.* **15**, 644 (2024).
61. M. Sun, B. Sun, M. Park, S. Yang, Y. Wu, M. Zhang, W. Kang, J. Yoon, L. Zhang, M. Sitti, Individual and collective manipulation of multifunctional bimodal droplets in three dimensions. *Sci. Adv.* **10**, eadp1439 (2024).
62. M. G. Worku, E. F. Enyew, Z. T. Desita, A. M. Moges, Sonographic measurement of normal common bile duct diameter and associated factors at the University of Gondar comprehensive specialized hospital and selected private imaging center in Gondar town, North West Ethiopia. *PLOS ONE* **15**, e0227135 (2020).
63. S. K. Lai, Y.-Y. Wang, D. Wirtz, J. Hanes, Micro- and macrorheology of mucus. *Adv. Drug Deliv. Rev.* **61**, 86–100 (2009).
64. T. Krings, J. Finney, P. Niggemann, P. Reinacher, N. Lück, A. Drexler, J. Lovell, A. Meyer, R. Sehra, P. Schauerte, M. Reinges, F. J. Hans, A. Thron, Magnetic versus manual guidewire manipulation in neuroradiology: In vitro results. *Neuroradiology* **48**, 394–401 (2006).
65. B. A. Gozen, O. B. Ozdoganlar, A rotating-tip-based mechanical nano-manufacturing process: nanomilling. *Nanoscale Res. Lett.* **5**, 1403–1407 (2010).
66. J. J. Abbott, E. Diller, A. J. Petruska, Magnetic methods in robotics. *Annu. Rev. Contr. Robot.* **3**, 57–90 (2020).
67. A. J. Petruska, B. J. Nelson, Minimum bounds on the number of electromagnets required for remote magnetic manipulation. *IEEE Trans. Robot.* **31**, 714–722 (2015).
68. M. Cai, Z. Qi, Y. Cao, X. Wu, T. Xu, L. Zhang, Development of reconfigurable electromagnetic actuation system with large workspaces: Design, optimization, and validation. *IEEE Trans Autom Sci Eng* **22**, 5982–5993 (2024).
69. O. Sen, P. K. Seshadri, N. K. Rai, J. Larentzos, J. Brennan, T. Sewell, C. R. Picu, H. S. Udaykumar, Johnson–Cook yield functions for cyclotetramethylene-tetranitramine (HMX) and cyclotrimethylene-trinitramine (RDX) derived from single crystal plasticity models. *J. Appl. Phys.* **135**, 145901 (2024).

Acknowledgments

Funding: This work was supported, in part, by the National Key R&D Program of China, grant 2023YFB4705600 (H.X.); the National Natural Science Foundation of China, grants 62422313 (X.F.), 92248302 (L.S.), and 61925304 (H.X.); the Max Planck Society (M.S.); and the European Research Council (ERC) Advanced Grant, SoMMoR Project, grant 834531 (M.S.). **Author contributions:** Conceptualization: X.F. and Q.C. Formal analysis: X.F., Q.C., Z.W., and D.T. Methodology: X.F., Q.C., and M.L. Data curation: X.F., Q.C., and D.T. Resources: Z.W., Q.C., and M.S. Investigation: X.F., Q.C., D.T., and Z.W. Software: X.F. and Q.C. Visualization: X.F., Q.C., and D.T. Validation: X.F. and M.L. Supervision: Z.Y., L.S., H.X., and M.S. Funding acquisition: X.F., L.S., and M.S. Project administration: Z.Y. and L.S. Writing—original draft: X.F., Q.C., and M.L. Writing—review and editing: X.F., Q.C., M.L., D.T., H.X., Z.W., Z.Y., L.S., and M.S. **Competing interests:** The authors declare that they have no competing interests. **Data and materials availability:** All data needed to evaluate the conclusions in the paper are present in the paper and/or the Supplementary Materials.

Submitted 20 January 2025
Accepted 2 June 2025
Published 4 July 2025
10.1126/sciadv.ads4411

Downloaded from https://www.science.org at Koc Universitesi Suna Kirac on December 05, 2025